Spectral energy distributions of classical cepheids in the magellanic clouds

Groenewegen, M.A.T.; Lub, J.

Astronomy & Astrophysics

Spectral energy distributions of classical Cepheids in the Magellanic Clouds[⋆,⋆⋆]

M. A. T. Groenewegen[1] and J. Lub[2]

[1] Koninklijke Sterrenwacht van België, Ringlaan 3, 1180 Brussels, Belgium
e-mail: martin.groenewegen@oma.be
[2] Leiden Observatory, Leiden University, PO Box 9513, 2300 RA Leiden, The Netherlands

ABSTRACT

In this study, we constructed spectral energy distributions (SEDs) for a sample of 142 Large Magellanic Cloud (LMC) and 77 Small Magellanic Cloud (SMC) fundamental-mode classical Cepheids (CCs) using photometric data from the literature. When possible, the data were taken to be representative of mean light or averaged over the light curve. The sample was built from stars that either have a metallicity determination from high-resolution spectroscopy or have been used in Baade-Wesselink types of analyses, or have a radial velocity curve published in *Gaia* DR3 or have Walraven photometry, or have their light- and radial-velocity curves modelled by pulsation codes. The SEDs were fitted with stellar photosphere models to derive the best-fitting luminosity and effective temperature. Distance and reddening were taken from the literature. Only one star with a significant infrared (IR) excess was found in the LMC and none in the SMC. IR excess in MW CCs is not uncommon suggesting that IR excess may be more prominent in MW cepheids than in the Magellanic Clouds. The stars were plotted in a Hertzsprung-Russell diagram (HRD) and compared to evolutionary tracks for CCs and to theoretical instability strips. For the large majority of stars, the position in the HRD is consistent with the instability strip. Period-luminosity (PL) and period-radius relations were derived and compared to these relations in the MW. For a fixed slope, the zero point of the bolometric PL relation does not depend on metallicity, contrary to recent findings of a significant metallicity term when considering the PL relation in different photometric bands. The mass-luminosity (ML) relation is derived and it points to an over luminosity of about +0.3 dex with respect to a canonical *ML* relation. The most intriguing result concerns the flux-weighted gravity (FWG, a quantity derived from gravity and effective temperature) and its relation to period and luminosity. Both relations agree with theory, with the results for the MW and with the independent estimates from the six known LMC eclipsing binaries that contain CCs. However, the FWG (as determined from dedicated high-resolution spectroscopy for the sample) is too low by about 0.8 dex in 90% of the cases. Recent works on time-series data on 20 CCs in the MW were analysed finding a similar (but less extreme) offset in gravity and the FWG. Most importantly, other time-series data on the same 20 CCs are in full agreement with the FWG-period relation. The observed time-series of spectroscopic data and from a two-dimensional hydrodynamical cepheid model was used to investigate the so-called effective gravity, that is, the gravity corrected for a dynamical term related to the time derivative of the radial velocity. There is a reasonable good correspondence between the predicted effective gravity and the observed gravity as a function of pulsation phase, which would potentially allow for an independent estimate of the projection factor, but the dynamical term is too small to explain the overall difference between the observed (flux-weighted) gravity and the (flux-weighted) gravity derived from the SED modelling and stellar mass estimates.

Key words. stars: distances – stars: fundamental parameters – stars: variables: Cepheids

1. Introduction

Classical Cepheids (CCs) serve as an important standard candle because they are bright and provide a link between the distance scale in the nearby Universe and that further out, via galaxies that contain both Cepheids and SNIa (see Riess et al. 2022 for a determination of the Hubble constant to 1.0 km s^{-1} precision). Typically, the period-luminosity (PL) relations of CCs that are at the core of the distance determinations are derived, namely: the photometric filters (V, I, K) or combination of filters that are designed to be independent of reddening, the so-called Wesenheit functions (Madore 1982); for example,

using combinations of (V, I), (J, K) or the combination used by the SH0ES team (F555W, F814W, and F160W HST filters, see Riess et al. 2022).

On the other hand, the bolometric magnitude or luminosity is a fundamental quantity of CCs as well as stars in general, as it is the output of stellar evolution models and the input to CC pulsation models. In Groenewegen (2020a, hereafter G20), the spectral energy distributions (SEDs) of 477 Galactic CCs were constructed and fitted with model atmospheres (and a dust component when required). For an adopted distance and reddening these fits resulted in a best-fitting bolometric luminosity (L) and the photometrically derived effective temperature ($T_{\rm eff}$). This allowed for the derivation of period-radius (PR) and PL relations, the construction of the Hertzsprung-Russell diagram (HRD), and a comparison to theoretical instability strips (ISs). The position of most stars in the HRD was consistent with theoretical predictions. Outliers were often associated with sources where the spectroscopically and photometrically determined effective

---

temperatures differed, or in cases where the sources exhibit a high degree of reddening with large uncertainties as well.

This sample was further studied in Groenewegen (2020b), where the relation between bolometric absolute magnitude and the flux-weighted gravity (FWG), defined as $\log g_{\mathrm{F}} = \log g - 4 \cdot \log\left(T_{\mathrm{eff}}/10^4\right)$ (Kudritzki et al. 2003), was investigated: the so-called flux-weighted gravity-luminosity relation (FWGLR). The tight correlation between g_{F} and luminosity was first demonstrated by Kudritzki et al. (2003, 2008) for blue supergiants (BSGs) and was later used for extra galactic distance determinations in Kudritzki et al. (2016). Anderson et al. (2016) then demonstrated that theoretical pulsation models for CCs also followed a tight FWGLR, one that is, in fact, tighter than the PL relation, finding that there was a good correspondence between observed g_{F} and period for a sample of CCs. Groenewegen (2020b) presented the currently best observationally determined FWGLR for Milky Way (MW) CCs, based on the luminosities derived in Groenewegen (2020a) and gravity and effective temperatures from the literature.

In Groenewegen (2020a) the adopted distances were based as much as possible on *Gaia* parallax data (from DR2 in that case). However, we need to correct the catalogued parallaxes for the parallax zero-point offset (PZPO). In GDR2, this value was −0.029 mas for quasars (Lindegren et al. 2018) and for CCs −0.046 ± 0.013 (Riess et al. 2018) or −0.049 ± 0.018 mas (Groenewegen 2018, hereafter G18), and was also a limiting factor in improving upon the local distance scale. In GEDR3 the *Gaia* team provided a Python script to the community (Lindegren et al. 2021, hereafter L21), which Riess et al. (2021) applied to a sample of 75 CCs in the MW, concluding that a counter correction of −14 ± 6 µas is required. The advantage of using the Magellanic Clouds (MCs) is that accurate and independently derived mean distances are available based on the analysis of samples of eclipsing binaries (Pietrzyński et al. 2019; Graczyk et al. 2020).

The present paper performs a study similar to Groenewegen (2020a) and Groenewegen (2020b) for a sample of CCs in the Small (SMC) and Large (LMC) Magellanic Clouds. The paper is structured as follows. In Sect. 2, the sample of 219 MC CCs is introduced, while Sect. 3 introduces the photometry that is used, the distances used, how the stellar mass is estimated and how the modelling of the SED is done. Section 4 offers a discussion of key results, in particular, the location of the CCs in the Hertzsprung-Russell diagram, the presence of any infrared excess, the period-radius and period-luminosity relations, the mass-luminosity relation, and the relation between the FWG and period and luminosity. A brief discussion and summary is given in Sect. 5.

2. Sample

In this paper, we study a sample of 142 LMC and 77 SMC CCs. Although this is a small subset of the about 4700 LMC and 4900 SMC CCs known in the MCs (see e.g. Ripepi et al. 2017, 2022), the stars in this sample are of special interest as they have been studied in other respects. Specifically, the sample is composed of: a) 89 LMC CCs for which Romaniello et al. (2022) derived iron and oxygen abundances (as well as effective temperatures and gravities) from high-resolution (HR) spectroscopy. This sample is composed of 68 CCs used to define the PL-relation in the LMC in the SH0ES program (Riess et al. 2019) and 21 for which archival spectra, first presented in Romaniello et al. (2008), were re-analysed; b) 14 SMC CCs

for which Romaniello et al. (2008) performed an abundance analysis. We note that for the LMC CCs in overlap Romaniello et al. (2022) derived an iron abundance that was (on average) 0.1 dex smaller compared to Romaniello et al. (2008); c) 7 CCs in the LMC cluster NGC 1866 (Molinaro et al. 2012; Lemasle et al. 2017) and four field SMC objects (Lemasle et al. 2017) with iron abundances from HR spectroscopy; d) CCs for which a Baade-Wesselink analysis has been carried out, in particular: 36 LMC and five SMC stars considered in Storm et al. (2011), and the almost identical sample of 36 LMC and six SMC stars analysed in Groenewegen (2013). Similarly, 27 LMC and eight SMC stars that have been analysed with the SPIPS code (Mérand et al. 2015) in Gallenne et al. (2017) to derive the pulsation (p) factor; e) CCs for which light-curves (and sometimes radial-velocity curves) have been fitted with theoretical pulsation models. In such a modelling (Marconi et al. 2013) the stellar mass, luminosity, and (mean) effective temperature are derived by fitting the light-curves (typical V, I, and K). The apparent distance moduli (DM) are derived from which the true DM and reddening are found. If RV curves are fitted, the projection-factor (p-factor) is also derived. Here, we consider the 11 LMC and 9 SMC fundamental-mode (FM) CCs studied in Ragosta et al. (2019) and Marconi et al. (2017), respectively; f) CCs with (previously unpublished) photometry in the Walraven (Walraven & Walraven 1960) system. This system is very usefull in constraining effective temperature and reddening as the photometric bands extend into the blue. van Genderen (1983) published VBLUW photometry for 21 SMC and 20 LMC CCs using data taken between 1971 and 1978 in South Africa (also see van Genderen 1981; Pel et al. 1981; van Genderen & Nitihardjo 1989). However, data collection continued from 1979 onwards from Chile and in Appendix A we report on these observations.

Furthermore, we have g) CCs in the MCs with RV curves published in *Gaia* DR3 (Ripepi et al. 2023; Gaia Collaboration 2023, 2016); h) SMC FM CCs for which UVES spectra and in part *HST* photometry will be obtained in the near future[1]. There are stars contained in the overlap between the different subsamples and the final sample consists of 142 LMC and 77 SMC CCs, all of which are FM pulsators. The basic parameters of the stars are compiled in Table 1.

3. Photometry, distance, masses, and modelling

3.1. Photometry

The SEDs were constructed using photometry retrieved mainly (but not exclusively) via the VizieR web-interface[2]. Data were considered (in increasing wavelength) in the UV from GALEX (Bianchi et al. 2017), in the optical from a variety of sources, namely, OGLE (B, V, I) photometry from Udalski et al. (1998) (SMC) and Udalski et al. (2000) (LMC), (V, I) photometry from the OGLE Shallow Survey in the LMC (Ulaczyk et al. 2012, 2013), and OGLE-IV data for both Clouds Soszyński et al. (2017), *Gaia* B_{p}, G, and R_{p} photometry from DR3 (Gaia Collaboration 2023), (B, R) photometry from the EROS survey in the LMC (Kim et al. 2014), (u, v, g, r, i, z) data from Skymapper DR2 (Onken et al. 2019), (B, V, R, I) photometry for LMC CCs from Sebo et al. (2002), (U,B,V) photometry

---

[1] See the publically available information on ESO program 0109.D-0846(A) (P.I. M. Romaniello) as per October 1st, 2022 and https://www.stsci.edu/hst/phase2-public/17097.pro (P.I. A. Riess), respectively.

[2] http://vizier.u-strasbg.fr/viz-bin/VizieR

Table 1. Sample of stars (selected entries).

Identifier	HV	Period (days)	d (kpc)	A_V (mag)	T_{eff} (K)	log g (cgs)	Ref	Luminosity ($L_\odot$)	T_{eff} (K)	R ($R_\odot$)	Mass ($M_\odot$)	log g (cgs)	log g_F (cgs)	χ^2_r
LMC0046	12717	8.844	50.62	0.39	5224 ± 134	2.45 ± 0.19	(5)	3777.1 ± 88.3	5750 ± 125	62.0 ± 2.7	5.50 ± 0.22	1.59 ± 0.04	2.55 ± 0.05	9.5
LMC0079	-1	22.544	50.52	0.36	6150 ± 97	1.50 ± 0.10	(4)	7823.3 ± 102.0	5125 ± 88	112.4 ± 3.8	6.58 ± 0.44	1.16 ± 0.04	2.32 ± 0.05	6.1
LMC0107	12452	8.739	50.48	0.43	5390 ± 42	0.80 ± 0.07	(1)	3834.1 ± 91.3	5750 ± 125	62.5 ± 2.7	5.68 ± 0.25	1.60 ± 0.05	2.57 ± 0.06	6.7
LMC0328	873	34.449	50.75	0.24	5222 ± 27	1.25 ± 0.06	(5)	17626.4 ± 335.4	5250 ± 144	160.8 ± 8.6	8.80 ± 0.40	0.97 ± 0.05	2.09 ± 0.07	7.0
LMC0367	872	29.822	49.79	0.24	5675 ± 120		(5)	9577.3 ± 137.1	5000 ± 125	130.6 ± 6.4	6.38 ± 0.56	1.01 ± 0.06	2.22 ± 0.07	16.7
LMC0434	875	30.349	50.25	0.26	5660 ± 100	0.30 ± 0.13	(2)	17254.3 ± 617.9	5625 ± 144	138.6 ± 7.3	7.22 ± 0.36	1.02 ± 0.05	2.02 ± 0.07	5.2
LMC0461	877	45.166	49.86	0.26	4890 ± 109	0.70 ± 0.08	(1)	14891.6 ± 257.9	4750 ± 125	180.5 ± 9.3	7.85 ± 0.70	0.82 ± 0.06	2.12 ± 0.08	13.6
LMC0467	876	22.720	49.70	0.23	5391 ± 74	1.63 ± 0.16	(5)	9500.7 ± 251.0	5375 ± 125	112.6 ± 5.3	6.54 ± 0.22	1.16 ± 0.05	2.23 ± 0.06	4.4
LMC0501	878	23.311	50.37	0.24	5130 ± 77	0.30 ± 0.05	(2)	10708.0 ± 279.0	5500 ± 125	114.2 ± 5.2	6.62 ± 0.12	1.14 ± 0.04	2.18 ± 0.05	4.6
LMC0504	12505	14.393	50.05	0.33				3867.4 ± 132.1	5000 ± 189	83.0 ± 6.1	5.63 ± 0.32	1.35 ± 0.07	2.55 ± 0.09	20.6
LMC0510	879	36.831	50.22	0.34	5530 ± 64	0.10 ± 0.15	(2)	13853.0 ± 335.2	4875 ± 153	165.3 ± 10.1	8.48 ± 0.53	0.93 ± 0.06	2.18 ± 0.08	33.5
LMC0512	2257	39.398	50.36	0.22	5200 ± 79	0.00 ± 0.09	(2)	17977.8 ± 152.2	5125 ± 88	170.4 ± 5.8	8.40 ± 0.48	0.90 ± 0.04	2.07 ± 0.05	6.2
LMC0528	881	35.731	50.47	0.15	5200 ± 64	0.10 ± 0.08	(2)	15023.5 ± 494.6	5125 ± 189	155.7 ± 11.2	7.70 ± 0.46	0.95 ± 0.07	2.11 ± 0.10	21.2
LMC0545	2262	15.832	50.38	0.25	5420 ± 85	0.80 ± 0.05	(2)	5898.8 ± 124.2	5250 ± 125	93.0 ± 4.4	6.52 ± 0.38	1.31 ± 0.05	2.43 ± 0.06	7.3
LMC0546	2249	15.216	49.64	0.21	6730 ± 285	1.40 ± 0.29	(5)	6215.9 ± 160.9	5500 ± 189	87.0 ± 5.8	5.99 ± 0.25	1.34 ± 0.06	2.38 ± 0.08	16.2
LMC0561	880	11.670	49.73	0.22	5383 ± 202	2.18 ± 0.26	(5)	4836.7 ± 88.8	5875 ± 168	67.2 ± 3.7	4.72 ± 0.15	1.45 ± 0.05	2.38 ± 0.07	7.1
LMC0590	882	31.787	50.18	0.31	5880 ± 322	0.00 ± 0.10	(2)	14075.5 ± 307.3	5250 ± 153	143.7 ± 8.2	7.48 ± 0.29	1.00 ± 0.06	2.12 ± 0.08	16.6
LMC0594	-1	6.733	50.19	0.27	5520 ± 194	0.90 ± 0.05	(2)	2245.8 ± 44.7	5625 ± 189	50.0 ± 3.2	4.90 ± 0.17	1.73 ± 0.06	2.73 ± 0.08	17.2
LMC0619	883	133.779	49.89	0.28	4754 ± 11	1.65 ± 0.02	(5)	48057.0 ± 2103.3	4625 ± 208	342.0 ± 29.8	8.03 ± 0.77	(0.27 ± 0.08)	(1.61 ± 0.11)	86.4
LMC0648	2270	13.626	50.17	0.28	5300 ± 90	0.50 ± 0.07	(2)	4192.2 ± 109.1	5250 ± 125	78.4 ± 3.7	5.53 ± 0.31	1.39 ± 0.05	2.51 ± 0.06	7.4
...														
SMC3533	1950	7.990	62.44	0.13	5900 ± 100	1.64 ± 0.10	(6)	3226.2 ± 123.4	5375 ± 189	65.6 ± 4.6	6.86 ± 0.89	1.65 ± 0.08	2.72 ± 0.10	24.8
SMC3565	1954	16.694	62.44	0.15	5890 ± 100	1.00 ± 0.10	(3)	9712.3 ± 285.1	5500 ± 153	108.7 ± 6.0	8.97 ± 0.66	1.32 ± 0.06	2.36 ± 0.08	13.8
SMC3588	1957	5.319	62.44	0.12	5975 ± 100	1.84 ± 0.10	(6)	1964.1 ± 75.0	5750 ± 189	44.7 ± 2.9	4.85 ± 0.27	1.83 ± 0.06	2.79 ± 0.08	16.0
SMC3611	1956	208.799	62.44	0.10	5677 ± 63	1.94 ± 0.19	(5)	69071.1 ± 2229.5	4375 ± 168	458.2 ± 34.0	9.60 ± 0.79	(0.10 ± 0.07)	(1.54 ± 0.10)	37.4
SMC4555	2209	22.642	62.44	0.17	6130 ± 100	1.10 ± 0.10	(3)	14112.7 ± 430.0	5625 ± 153	125.3 ± 6.8	8.64 ± 0.08	1.18 ± 0.04	2.18 ± 0.06	18.0
SMC4697	817	18.901	62.44	0.12	5850 ± 100	1.00 ± 0.10	(3)	9953.4 ± 533.2	5500 ± 237	110.1 ± 9.4	7.91 ± 0.35	1.26 ± 0.08	2.30 ± 0.11	59.7
SMC4919	6357	33.338	62.44	0.18	6130 ± 100	0.50 ± 0.10	(3)	21581.7 ± 924.8	5250 ± 204	177.9 ± 13.6	11.61 ± 0.24	1.00 ± 0.07	2.12 ± 0.09	13.5
SMC4953	11211	21.386	62.44	0.09	4830 ± 100	0.00 ± 0.10	(3)	11665.8 ± 387.5	5250 ± 153	130.8 ± 7.6	10.08 ± 0.59	1.21 ± 0.06	2.33 ± 0.08	15.8
SMC4976	2231	36.737	62.44	0.17				16641.3 ± 1921.0	5125 ± 312	163.9 ± 20.5	8.38 ± 0.55	0.93 ± 0.11	2.09 ± 0.15	47.9

Notes. Column 1. The identifier used in this paper, which is related to the identifier used by OGLE. The first entry, LMC0046, for example, would be known as OGLE-LMC-CEP-0046. Column 2. Harvard variable (HV) identifier, when available. Column 3. Pulsation period. Column 4. The adopted distance. For the LMC objects this includes the geometric correction, see Sect. 3.2. Column 5. The adopted reddening value A_V based on Skowron et al. (2021), see main text. Column 6. Effective temperature in the literature. For references 3 and 6 an uncertainty of 100 K has been adopted. Column 7. log gravity in the literature. For references 3, 4 and 6 an uncertainty of 0.1 dex has been adopted. Column 8. References for the data in Cols. 6 and 7, (1) Romaniello et al. (2022), re-analysed data from Romaniello et al. (2008). (2) Romaniello et al. (2022; new spectra, Tables 3 and 5), (3) Romaniello et al. (2008), (4) Lemasle et al. (2017), (5) Sprague et al. (2022). (6) Ragosta et al. (2019; LMC) and Marconi et al. (2017; SMC). For reference (6) the values are not determined from high-resolution spectroscopy but from their best-fitting LC fitting models. Column 9. Luminosity with error bar from the SED fitting. Column 10. (photometric) effective temperature with error bar from the SED fitting. Column 11. Radius with error bar, derived from L and T_{eff}. Column 12. Adopted stellar mass, see Appendix B. Column 13. log gravity determined from mass and radius. Column 14. Flux-weighted gravity calculated from the gravity and T_{eff}. For a few stars the mass estimate is clearly too low given their period and the value for the mass and (flux-weighted) gravity are not used and listed between parenthesis. Column 15. The reduced χ^2 of the fit to the SED. The full table is available at the CDS.

from Madore ([1975](#)), Eggen ([1977](#)), and Martin & Warren ([1979](#)), Walraven (VBLUW) photometrey (see Appendix A), (U, B, V, I, K) for CCs in NGC 1866 from Musella et al. ([2016](#)), HST F555W, F814W, and F160W photometry from Riess et al. ([2019](#)) for LMC Cepheids, and further to the near- and mid-infrared, (Y, J, K) photometry from the VMC survey (Cioni et al. [2011](#)) for the SMC (Ripepi et al. [2016](#)) and LMC (Ripepi et al. [2022](#)), and from the public DR6 for a few remaining stars, (J, H, K) photometry for LMC CCs from Persson et al. ([2004](#)) and Macri et al. ([2015](#)), Akari photometry for the SMC (Ita et al. [2010](#)) and LMC (Kato et al. [2012](#)). We note that for the S7, S11, and L15 filters, only errors in the magnitudes of <0.15, <0.20, and <0.20 mag, respectively, were accepted. Then, we also used AllWISE photometry (Cutri & et al. [2014](#); in the W3 and W4 filters only errors in the magnitudes of <0.30, and <0.25 mag, respectively, were accepted), *Spitzer* IRAC photometry from Chown et al. ([2021](#); mean magnitudes from template fitting in the 3.6 and 4.5 μm bands) and from VizieR catalogue II/305/catalog in the 5.8 and 8.5 μm bands. Finally, we used MIPS photometry at 24 μm available from the IRSA[3]. No MIPS data at 70 μm were available.

The number of available photometric data points for the LMC CCs ranges from 16 to 39, with a median of 30, and for the SMC objects from 15 to 29, with a median of 20 photometric points. The data contain single-epoch observations (typically from GALEX and Akari) but whenever possible values at mean light were taken or multiple datapoints were averaged.

3.2. Distance and geometric correction

The mean distance to the LMC is adopted to be d_{LMC} = 49.59 ± 0.09 (stat) ± 0.54 (syst) kpc (Pietrzyński et al. [2019](#)), and to the SMC of d_{SMC} = 62.44 ± 0.47 (stat.) ± 0.81 (syst.) kpc (Graczyk et al. [2020](#)), based, in both cases, on the analysis of samples of eclipsing binaries. The depth effect in the SMC is considerable, for example Ripepi et al. ([2017](#)), but all SMC sources have been adopted to be at the mean distance. For the LMC the first order approximation of an inclined disk is adopted to compute the geometric correction and the procedure in Riess et al. ([2019](#)) is followed, taking the inclination and position angle of the line of nodes of the disk from Pietrzyński et al. ([2019](#)) and the LMC center-of-mass coordinates from van der Marel & Kallivayalil ([2014](#)). The adopted distances are listed in Col. 4 in Table 1.

3.3. Stellar masses

An estimate for the stellar mass is required when computing the stellar gravity, with the stellar radius available from the best-fitting luminosity and effective temperature combination, as detailed below. Several methods have been employed to this end. First, the period-luminosity-mass-effective temperature-metallicity relation derived in Groenewegen & Jurkovic ([2017](#)) based on the models of Bono et al. ([2000b](#)).

Alternatively, and in a similar way, such a relation was derived here based on the models of Anderson et al. ([2016](#)). That paper gives, for a given mass, metallicity and rotational speed – the period, luminosity, and effective temperature at the start and end of the IS, and for different crossings of the IS a star may undergo. As the first-crossing is very short compared to the other crossings these models were not considered. An initial fit showed that the metallicity term is not significant. The best

linear fit for average rotation, all metallicities, and the second and third crossing models for FM pulsators is:

$$\log P = (13.095 \pm 0.114) + (0.857 \pm 0.010) \log L$$
$$- (0.669 \pm 0.032) \log M - (3.912 \pm 0.030) \log T_{eff}$$
$$(N = 46, \sigma = 0.0076). \quad (1)$$

Based on the model fitting of LMC Cepheid light curves Ragosta et al. ([2019](#)) presented a period-mass-radius relation of

$$\log P = (-1.618 \pm 0.007) + (-0.68 \pm 0.02) \log M$$
$$+ (1.72 \pm 0.01) \log R \quad (2)$$

with a dispersion of only 0.005 dex. This relation will be applied to the SMC ones as well.

Pilecki et al. ([2018](#)) analysed the light- and radial-velocity curves of the six known cepheid containing eclipsing binaries (containing seven Cepheids, including one type-II cepheid (T2C), all in the LMC). For convenience, the stellar parameters they derived for the Cepheids are compiled in Table 2, as they appear in several plots. Pilecki et al. ([2018](#)) derived the following period-mass-radius relation

$$\log P = (-1.555 \pm 0.035) - (0.795 \pm 0.044) \log M$$
$$+ (1.703 \pm 0.023) \log R \quad (3)$$

with a dispersion of 0.037 dex. This relation will be applied to the SMC ones as well. The mass range on which this relation is based is smaller than that of the other relations.

Marconi et al. ([2020](#)) used nonlinear convective pulsation models to link period and mass to a Wesenheit index based on *Gaia* magnitudes. For a mixing length parameter of 1.7 and FM pulsators Marconi et al. ([2020](#)) give:

$$WG - DM = -1.686 - 2.496 \log P - 2.285 \log M \quad (4)$$

with a dispersion of 0.058 mag, and where $WG = G - 1.90 \cdot (B_p - R_p)$ (Ripepi et al. [2019](#)) and DM is the distance modulus. The pulsation models were calculated at solar metallicity but will be used for the MC CCs.

The mass estimates from these five methods are listed in Table B.1. The adopted mass is the median among the five estimates, and is listed in Table B.1 and in Col. 12 in Table 1. To estimate the error bar, the error in the mass estimate of the median value is added in quadrature to the median-absolute-deviation times 1.48 (to get the equivalent of one sigma in a Gaussian distribution) among the five estimates.

The different estimates are in good agreement in most cases, except for some of the longest period Cepheids where some individual estimates give unrealistically low masses, leading to the median value becoming also unrealistically low. These values are set between parenthesis and have not been used in the analysis. The origin of the discrepancy is probably related to the fact that the different mass-estimate formalisms are not derived from such long-period Cepheids.

3.4. Modelling

The SEDs are fitted with the code More of DUSTY (MoD, Groenewegen [2012](#))[4] which uses a slightly updated and modified version of the DUSTY dust radiative transfer (RT) code (Ivezić et al. [1999](#)) as a subroutine within a minimisation code. As we

---

[3] https://irsa.ipac.caltech.edu/applications/Gator/, "SAGE MIPS 24 um Epoch 1 and Epoch 2 Full List."

[4] http://homepage.oma.be/marting/codes.html

Table 2. Stellar parameters of the Cepheid in known LMC EBs (from Pilecki et al. 2018).

Name	Period (days)	M_1 ($M_\odot$)	$\log g_1$ (cgs)	T_{eff1} (K)	$\log L_1$ ($L_\odot$)	R_1 ($R_\odot$)	p_f	Remarks
CEP0227	3.79708	4.15 ± 0.03	1.970 ± 0.004	6000 ± 160	3.15 ± 0.05	34.87 ± 0.12	1.21 ± 0.05	
CEP4506	2.98785	3.61 ± 0.03	2.087 ± 0.007	6120 ± 160	3.01 ± 0.05	28.5 ± 0.2	1.35 ± 0.09	
CEP2533	2.833	3.98 ± 0.10	2.10 ± 0.04	6350 ± 150	3.10 ± 0.06	29.2 ± 1.4		FO
CEP1812	1.31290	3.76 ± 0.03	2.509 ± 0.007	6120 ± 150	2.61 ± 0.04	17.85 ± 0.13	1.26 ± 0.08	
CEP1718	2.732	4.27 ± 0.04	2.18 ± 0.04	6310 ± 150	3.04 ± 0.06	27.8 ± 1.2		FO
CEP1718	3.460	4.22 ± 0.04	2.02 ± 0.03	6270 ± 160	3.18 ± 0.06	33.1 ± 1.3		FO
T2C098	4.97372	1.51 ± 0.09	1.81 ± 0.03	5300 ± 120	2.66 ± 0.04	25.3 ± 0.2	1.30 ± 0.05	

Notes. Column 1. Name/identifiers. CEP0227 refers to OGLE-LMC-CEP-0227, etc. T2C098 refers to LMC-T2CEP-098. CEP1718 appears twice as both components of the EB are Cepheids. Column 2. FM Period. For the first overtone (FO) pulsators the conversion is outlined in Pilecki et al. (2018). Columns 3–7: Stellar parameters of the cepheid: mass, gravity, effective temperature, luminosity and radius. Column 8. Projection factor when available. Column 9. Remarks, indicating which Cepheids are FO pulsators. All data from Pilecki et al. (2018).

are not interested in any dust component the dust optical depth is initially set to zero. In that case, the input to the model are the distance, reddening, and a model atmosphere. The few cases where an infrared (IR) excess may be present are discussed in Sect. 4.3.

The model atmosphere fluxes are reddened to be compared to the observations. The reddening map of Skowron et al. (2021) for the MCs is adopted and the $E(V - I)$ value in the map closest to the source is taken. The visual extinction is then assumed to be $A_V = 3.1 \cdot E(V - I)/1.318$, and is listed in Col. 5 in Table 1.

MARCS model atmospheres are used as input (Gustafsson et al. 2008) for $\log g = 1.5$ and metallicity -0.50 and -0.75 dex for the LMC and SMC stars, respectively. The model grid is available at 250 K intervals for the effective temperature range of interest, and adjacent model atmospheres are used to interpolate models at 125 K intervals, which better reflects the accuracy in T_{eff} that can be achieved. For every model atmosphere (that is, T_{eff}) a best-fitting luminosity (with its (internal) error bar, based on the covariance matrix) is derived with the corresponding reduced χ^2 (χ_r^2) of the fit. The model with the lowest χ_r^2 then gives the best-fitting effective temperature. Considering models within a certain range above this minimum χ_r^2 then gives the estimated error in the effective temperature and luminosity. For the luminosity, this error is added in quadrature to the internal error in luminosity.

The best fitting effective temperature and luminosity with error bar are listed in Cols. 9 and 10, and the resulting radius in Col. 11 of Table 1. Combined with the mass this gives the gravity (Col. 13), and gravity combined with T_{eff} the FWG (Col. 14).

4. Results and discussion

4.1. General

Figures 1 and D.1 present the four best, respectively, the four poorest fits to the SEDs (according to the χ_r^2), respectively, with the residual (model minus observations) in the bottom part of each panel[5]. In the model fitting procedure photometric outliers were excluded in the following way. The rms in the residuals was determined and added in quadrature to the photometric error bar for each data point. If the absolute difference between model and observations was larger than 4σ the point is flagged and plotted

with an error bar of 3.0 mag to still identify it but to have no influence on the fitting.

The fits are quite acceptable. In the poorest fits the scatter among the various photometric points is larger overall. In the case of SMC0417 and SMC0921 this leads to the result that the most visually discrepant points (the VMC JHK points) are not marked as 4σ outliers and that therefore the reduced χ^2 is large.

A limitation of our procedure is that time variability of the photometry is not taken into account. Values at mean light have been considered whenever possible, but the SEDs also contain single-epoch data. Pulsation amplitudes decrease with wavelength so the effect should not play a major role in the mid and far-IR and in the NIR where the SEDs peak mean-light magnitudes are typically available. The construction of the SED at mean light also ignores possible phase shifts between photometric bands.

We have compared our results to the fully independent modelling by Gallenne et al. (2017) using the SPIPS code (Mérand et al. 2015) for 35 stars in overlap. The SPIPS code takes light curves as input and therefore considers the time variability. It is also independent in the sense that it fits ATLAS9 model atmospheres (Castelli & Kurucz 2003).

Figure 2 compares the result and the agreement is excellent. The rms in the residuals is about 160 K in T_{eff} and 0.05 dex in $\log L$. The effective temperature plot suggest that the errors in effective temperature may have been overestimated by about $\sim 40\%$ in both studies.

4.2. Hertzsprung-Russell diagram

Figure 3 shows the HRD together with sets of evolutionary tracks and ISs. Objects from the sample are plotted as black (LMC) and red (SMC) open squares, respectively. Stars located outside the bulk of objects are plotted with error bars, and some are labelled as well. Blue symbols with error bars indicate the six CCs in EBs (three FM as filled squares, three FO as filled triangles; see Table 2).

Two sets of ISs from De Somma et al. (2021) (at brighter magnitudes) and from Pilecki et al. (2018) (at fainter magnitudes) are plotted. The near horizontal green lines indicate the evolutionary tracks for $Z = 0.006$ and average initial rotation rate $\omega_{\text{ini}} = 0.5$ from Anderson et al. (2016). Increasing in luminosity are tracks for initial mass (number of the crossing through the IS): 4 (1), 5 (1), 7 (1), 7 (2), 7 (3), 9 (1), 9 (2), 9 (3), 12 (1), and 15 $M_\odot$ (1). The density of stars in the HRD is qualitatively

---

[5] The complete set of SEDs is available at https://doi.org/10.5281/zenodo.8032168
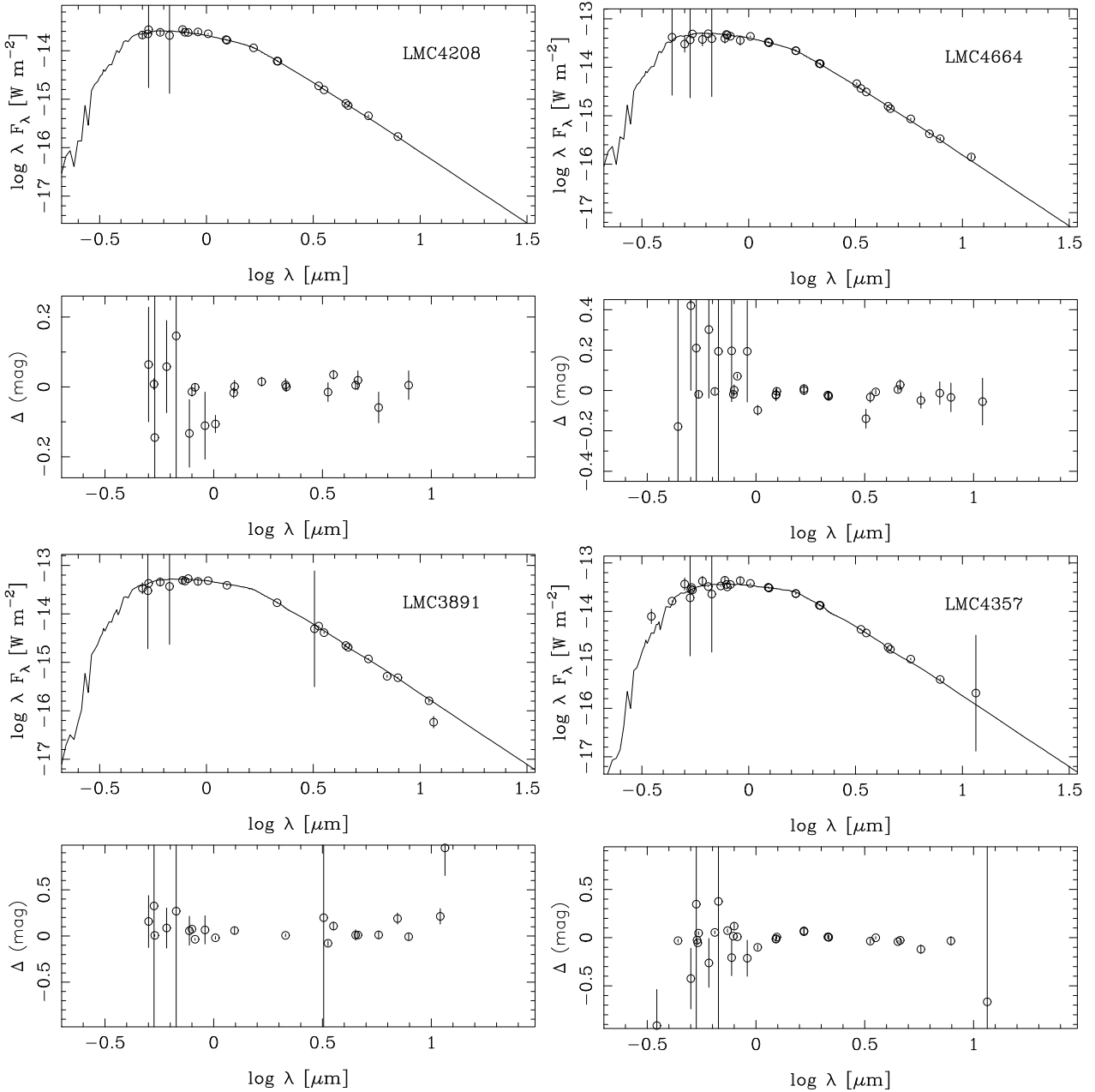
Fig. 1. Four best-fitting models. The upper panels: Observations (with error bars) and the model. The lower panels: Residuals. Outliers that have been clipped are plotted with an (arbitrary) error bar of 3.0 mag.

consistent with the fact that the first crossing is much faster than the second and third crossings.

There are only two clear outliers, LMC1940 and LMC1945, and their position in the HRD remains unexplained. The former object has the fourth poorest fit, but the χ_r^2 of the fit of LMC1945 is not extremely poor. LMC1940 and LMC1945 have large *Gaia* `astrometric_gof_al` (GoF) parameters of about 12 and 9.9, respectively (and `RUWE` values of 1.56 and 1.43, respectively), which may hint to binarity. However, 38 stars in the sample have a larger GoF than 9.9 and are not outliers in the HRD diagram. A cautionary note is that the SED fitting assumes the stars to be single. Contamination of the photometric points by a companion will have an influence on the results of the fitting procedure. No spectroscopic temperature determinations is available for LMC1945. For LMC1940 there is a value of 4909 ± 126 K determined from APOGEE data (Sprague et al.

2022). A model with 4875 K (the closest in the available grid) was run to find that the luminosity is about 13% less than in the best-fitting model. This temperature and luminosity would put the star closer to the red edge of the IS, but still too cool and overly under-luminous, compared to expectations.

The location of the known CCs in EBs in noteworthy. Five of them are clearly hotter than expected from the IS by De Somma et al. (2021) but are consistent with the IS as calculated by Pilecki et al. (2018). It is noted that the effective temperatures in Pilecki et al. (2018) have not been derived from the available (disentangled) spectra that these authors used to obtain the radial velocities, but from effective temperature–colour relations using the $V - I$ (sometimes $V - K$) colour of the two components, as derived from the modelling of the light curve. This may have possibly introduced a systematic effect. If the temperatures derived in this way would end up being too high, the luminosities

Table 3. Effect of dust on the colours of CCs.

Name	$T_{\rm eff}$ (K)	L ($L_\odot$)	BIC	Bp (mag)	G (mag)	Rp (mag)	V (mag)	I (mag)	J (mag)	K (mag)	F160W (mag)	WG (mag)	WVI (mag)	WJK (mag)	WH (mag)
LMC0619	4625	48057 ± 1645	2809	12.37	11.71	11.12	12.27	10.97	10.18	9.45	9.67	9.34	8.96	8.95	9.18
	4750	45036 ± 946	713	12.42	11.79	11.20	12.30	11.06	10.30	9.60	9.81	9.47	9.14	9.12	9.35
		$T_{\rm c}$ = 535 ± 26 K		−0.05	−0.08	−0.08	−0.03	−0.09	−0.12	−0.15	−0.14	−0.13	−0.18	−0.17	−0.17
LMC1616	4875	4026 ± 85	752	14.88	14.30	13.75	14.78	13.62	12.92	12.28	12.47	12.15	11.82	11.84	12.03
	4875	4185 ± 91	614	14.93	14.34	13.77	14.81	13.64	12.91	12.25	12.45	12.14	11.83	11.79	12.01
		$T_{\rm c}$ = 329 ± 40 K		−0.05	−0.04	−0.02	−0.03	−0.02	+0.01	+0.03	+0.02	+0.01	−0.01	+0.05	+0.02
LMC0966	5000	21971 ± 379	971	12.99	12.44	11.92	12.89	11.79	11.13	10.54	10.71	10.41	10.08	10.13	10.29
	5000	21876 ± 387	885	13.02	12.46	11.92	12.90	11.80	11.14	10.55	10.71	10.37	10.10	10.14	10.29
		$T_{\rm c}$ = 417 ± 125 K		−0.03	−0.02	+0.00	−0.01	−0.01	−0.01	−0.01	+0.00	+0.04	−0.02	−0.01	+0.00
SMC1172	5250	4960 ± 83	214	14.97	14.50	14.02	14.89	13.89	13.31	12.79	12.93	12.69	12.34	12.43	12.55
	5500	5958 ± 182	130	14.96	14.52	14.05	14.87	13.94	13.30	12.77	12.93	12.79	12.50	12.40	12.58
		$T_{\rm c}$ = 90 ± 7 K		+0.01	−0.02	−0.03	+0.02	−0.05	+0.01	+0.02	+0.00	−0.10	−0.16	+0.03	−0.03
LMC0107	5750	3834 ± 31	55	14.89	14.46	14.01	14.81	13.89	13.35	12.92	13.04	12.79	12.46	12.62	12.69
	5875	4047 ± 39	60	14.88	14.46	14.01	14.79	13.90	13.36	12.94	13.06	12.81	12.52	12.65	12.73
		$T_{\rm c}$ = 217 ± 28 K		+0.01	+0.00	+0.00	+0.02	−0.01	−0.01	−0.02	−0.02	−0.02	−0.06	−0.03	−0.04
LS Pup	5500	4395 ± 152	3436	10.49	9.76	9.11	10.39	8.94	8.08	7.43	7.67	7.14	6.69	6.98	7.13
	5750	4364 ± 153	2752	10.55	9.81	9.15	10.45	8.97	8.05	7.40	7.65	7.15	6.68	6.95	7.10
		$T_{\rm c}$ = 3620 ± 1182 K		−0.06	−0.05	−0.04	−0.06	−0.03	+0.03	+0.03	+0.02	−0.01	+0.01	+0.03	+0.03

Notes. For every star the first line gives the best-fitting parameters based on the model atmosphere, the second line when including a dust component, and the third line the difference in magnitude. In the column of the luminosity the dust temperature at the inner radius ($T_{\rm c}$) is listed in the third line. W refers to the Wesenheit magnitudes, defined as follows: $WG = G − 1.90 \cdot (Bp − Rp)$, $WVI = I − 1.55 \cdot (V − I)$, $WJK = K − 0.69 \cdot (J − K)$, $WH =$ F160W $−0.386 \cdot$ (F555W − F814W). Note that F555W and F814W magnitudes are not explicitly listed in the table (they are close to V and I) but were calculated and used in calculating the WH magnitude.
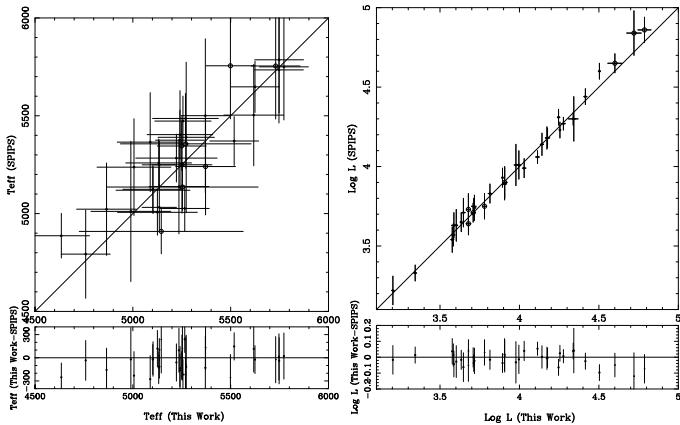
Fig. 2. Comparison of effective temperature and luminosity between the present work and the 27 LMC (filled circles) and 8 SMC (open circles) stars in overlap. The bottom panels show the residuals.

would also be too large, as indeed inferred from the PL-relation (see below).

4.3. Infrared excess

The default assumption in the modelling has been that there is no IR excess and the SEDs can be modelled by a stellar atmosphere. However, near- and mid-IR excess is known to exist in Galactic CCs, for example, direct interferometric observations in the optical or NIR (e.g. Kervella et al. 2006; Mérand et al. 2006; Gallenne et al. 2012; Nardetto et al. 2016), modelling with the SPIPS code (e.g. Breitfelder et al. 2016; Trahin 2019; Trahin et al. 2021, and Gallenne et al. 2017 for the LMC) and was also found in modelling the SEDs of Galactic CCs (Gallenne et al. 2013, G20).

Visual inspection of the SEDs showed five cases where an IR excess could explain the shape of the SEDs[6]. Following G20, models were run for these five stars including a dust component and additionally fitting for the dust temperature at the inner radius and the dust optical depth under the assumption of spherical symmetry. Following G20, a mixture of 3% silicate, 3% aluminium oxide and 94% iron dust was adopted. The analysis of the MW CCs in G20 with available mid-IR spectra showed that these are near featureless requiring a large fraction of featureless iron dust, although the nature of the excess is in fact unclear. The results of the fitting are listed in Table 3 that include the magnitudes in various filters for the best-fitting model excluding and including a dust component.

Only the model for LMC0619 is convincing with an excess in four to five filters (see Fig. 4) and an SED comparable in shape to the SEDs of the MW CCs with IR excess. In the other four cases, the temperature at the inner radius is very low and based on two filters only (see Fig. D.2). Also, the reduction in the Bayesian information criteria (BIC) is small.

Interestingly, the best-fitting model with dust predicts fainter magnitudes for LMC0619. For fixed effective temperature and luminosity and for optically thin cases, one expects some absorption in the optical and emission in the IR. However, in the fitting the effective temperature and luminosity were allowed to vary, and the best-fitting luminosity is lower when including dust. The difference in the Wesenheit filters is around 0.15 mag, which is significant.

Only one of 142 CCs in the LMC, and 0/77 in the SMC has a convincing IR excess. Coincidence or not, LMC0619 has the longest period of the LMC objects (133 days) and one of the

---

[6] Cases where the excess consisted only in a single point, typically in the WISE3 filter are not discussed here. They are probably related to contamination in the larger W3 (and W4) beams. An a-priori selection on photometric error in the W3 and W4 filters was applied (Sect. 3.1) but this did not remove all likely unreliable points. The stars discussed in the main text appear to have IR excess in multiple filters.
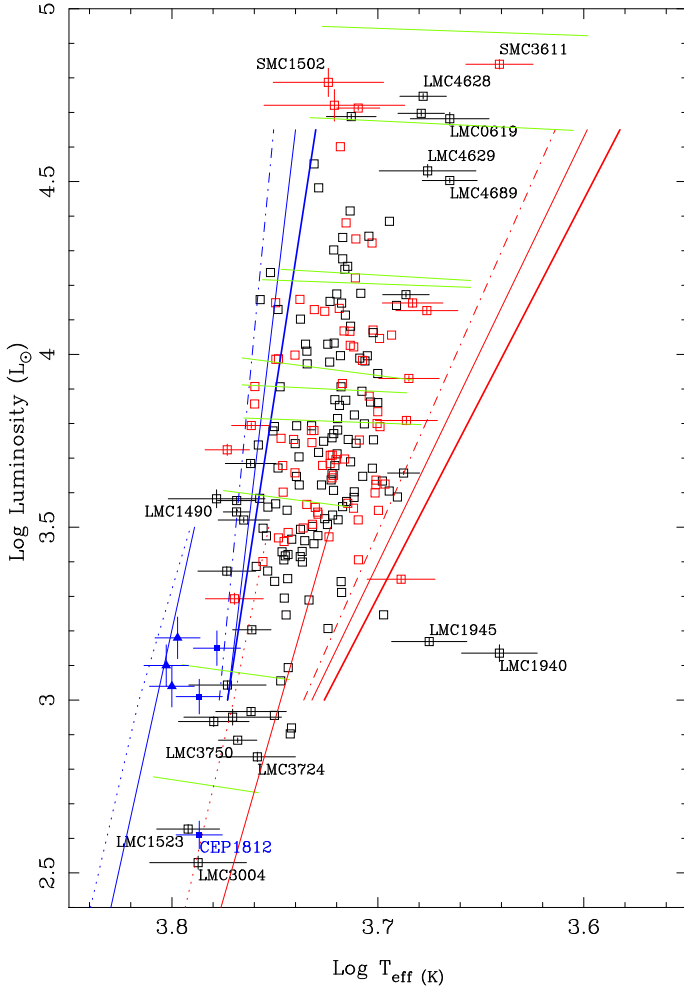
Fig. 3. Hertzsprung-Russell diagram. Black and red open squares indicate LMC and SMC CCs from the sample, respectively. Stars located outside the bulk of objects are plotted with error bars, and some are labelled as well. Blue symbols with error bars indicate the six CCs in EBs (three FM as filled squares, three FO as filled triangles, see Table 2). Blue and red lines indicate the blue and red edge of the IS. In the upper part (brighter than $\log L = 3$), the results from De Somma et al. (2021) are plotted. The thinner solid and dot-dashed line are for $Z = 0.008$ and $Z = 0.004$ models, respectively, for their type A mass-luminosity relation. The tick line is for $Z = 0.008$ for their type-B mass-luminosity relation. In the lower part (fainter than $\log L = 3.5$), the results from Pilecki et al. (2018) are plotted for FM (solid lines) and FO (dotted lines) model. Green lines indicate evolutionary models from Anderson et al. (2016). See the main text for details.

4.4. Period-luminosity relations

Figure 5 shows the PL relation. A fit to 141 LMC objects (removing one object through 3σ clipping) is:

$$M_{\rm bol} = (-2.96 \pm 0.05)\log P + (-1.10 \pm 0.05) \qquad (5)$$

with an rms of 0.20 mag. A fit to 77 SMC objects (removing zero outliers) is:

$$M_{\rm bol} = (-3.04 \pm 0.11)\log P + (-0.99 \pm 0.14) \qquad (6)$$

with an rms of 0.25 mag.

LMC1940 is an outlier in the HRD, but also in the PL-relation. Its period would suggest $M_{\rm bol} \approx -4.0$, or $\log L \approx 3.5$. In the HRD, this would move the star up but it would still be an outlier and too cool for its expected position. Although it is underluminous for a CC LMC1940 is too luminous to be a Type-II cepheid (T2C), as indicated by the PL-relation for T2Cs from Groenewegen (2020a). We also note that the CCs in EBs are slightly brighter than the mean relation.

In G20 the slope and the zero point (ZP) based on 380 Galactic CCs were derived to be -2.95 ± 0.09 and -0.98 ± 0.07 (rms of 0.40 mag), respectively. The slopes derived for the three galaxies agree to within the error bar. Fixing the slope to the most precise one of that in the LMC (-2.96), ZPs of -4.057 ± 0.002 and -4.046 ± 0.004 are found for LMC and SMC at $\log P = 1$, respectively.

The bolometric PL relation to the Galactic Cepheids presented in G20 did not select based on metallicity. Figure D.3 shows the distribution in [Fe/H] of the stars that went into that fitting. The 5–95% range is from -0.31 to $+0.29$ dex, with a median of $+0.06$. Selecting stars in the range $0.0 \leq$ [Fe/H] $<+0.2$ to better have a sample of near solar metallicity leads to a median of $+0.09$ (with 0.06 dex dispersion[7]) and a PL-relation of

$$M_{\rm bol} = (-2.64 \pm 0.11)\log P + (-1.34 \pm 0.09) \qquad (7)$$

with an rms of 0.35 mag using 191 stars, and a ZP of -4.041 ± 0.002 at 10 days for a fixed slope of -2.96.

Figure 6 shows the ZP at 10 days plotted against metallicity. The metallicity for the MW is the one just derived, for the LMC -0.409 dex with dispersion of 0.076 (Romaniello et al. 2022) is adopted and for the SMC, a value of -0.75 dex with dispersion of 0.08 (Romaniello et al. 2008) is assumed. A least-squares fit taking into account the error bars in both axes gives

$$\text{ZP@10d} = (-4.0451 \pm 0.0036) + (+0.0082 \pm 0.0075) \cdot \text{[Fe/H]} \qquad (8)$$

Using slightly different values for the LMC, for example, -0.35 ± 0.09 dex for BSGs (Urbaneja et al. 2017), or -0.62 ± 0.14 dex for SMC cluster giants (Trundle et al. 2007, as quoted in Romaniello et al. 2008) all lead to slight positive but insignificant slopes. A constant value of -4.049 mag with dispersion 0.008 mag would fit the ZPs of all three galaxies.

The result that the bolometric PL relation does not seem to depend on metallicity is in contrast with the most recent results of Breuval et al. (2022) that derive the metallicity term in various filters from *Gaia* Bp band to IRAC 4.5 μm and find little dependence on wavelength and an average of $\gamma = -0.29$ mag dex^{-1}. Our results indicate that the LMC Cepheids are indeed brighter

highest luminosities. In the MW, IR excess is quite common (see references at the beginning of the section) and G20 lists 16/347 stars as having an IR excess, also based on SED fitting. It appears that the presence of IR excess is more common in the MW than in LMC and SMC CCs For comparison, one of the MW stars with IR excess from G20, LS Pup, was refitted and the results are included in Table 3 and Fig. D.2. A definite conclusion would require a more in debt study beyond the scope of the present paper, as one would have to consider the impact of the bias due to the fact that for MW CCs more data is available (in some cases even mid-IR spectra) especially at longer wavelengths. The SED modelling is therefore more likely to find an IR excess in MW stars than in the MCs.

---

[7] Calculated as 1.48 times the median absolute deviation.
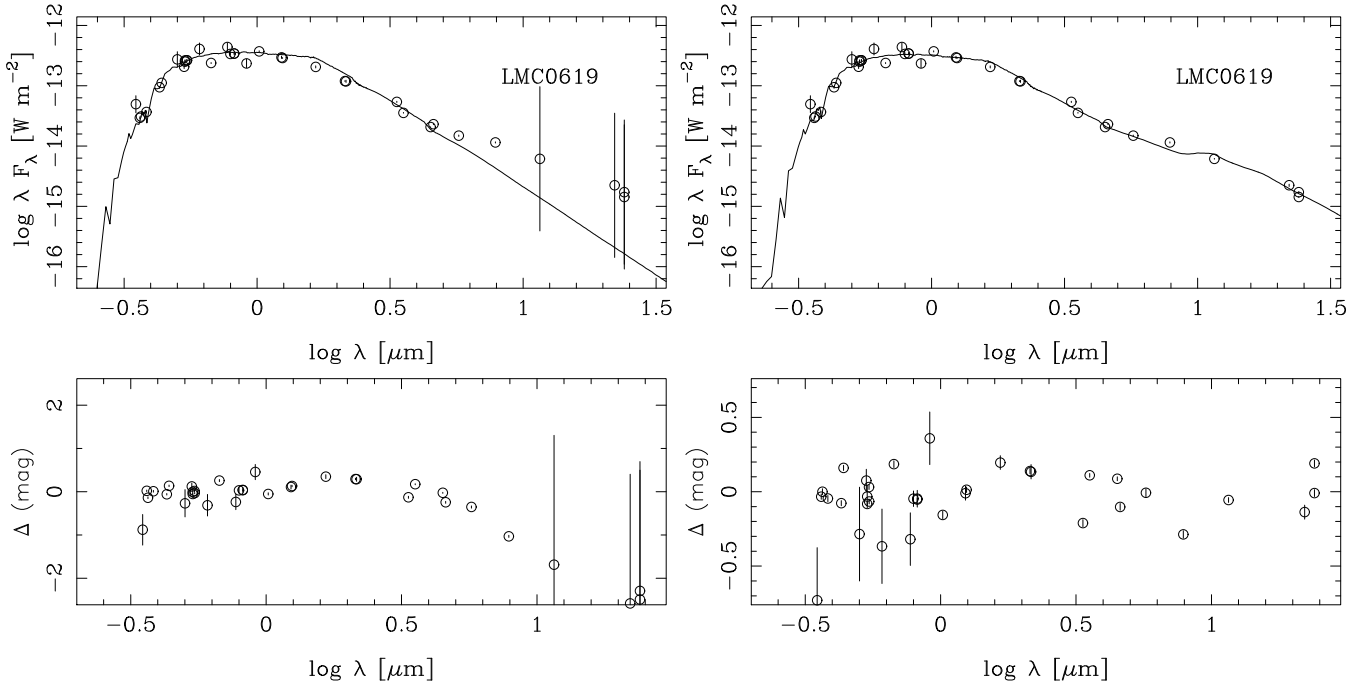
Fig. 4. Best-fitting model without dust (left side) and with dust (right side) for the star with the most convincing presence of an IR excess. In the model without dust, the long-wavelength points are considered outliers.
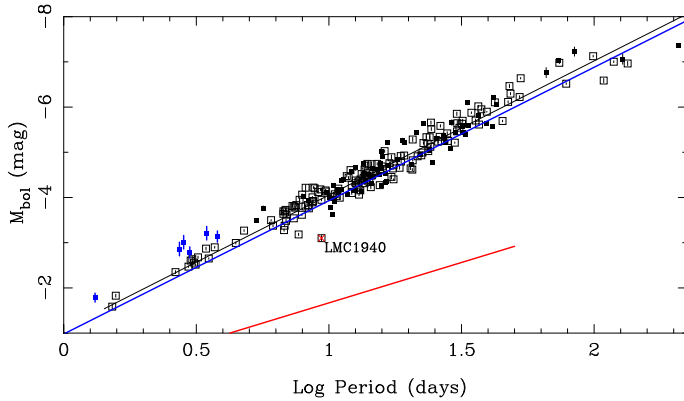
Fig. 5. Period-M_{bol} relation. Error bars in M_{bol} are plotted but are typically smaller than the symbol size. LMC objects are plotted as open squares, SMC objects are filled squares. Blue symbols indicate the six CCs in EBs. One outlier is marked by a red cross and is identified. The black line indicates the best fit (excluding the outlier) to the complete MC sample. Fits to the LMC and SMC stars separately are given in the text. The blue line gives the PL relation for MW CCs from G20, while the red line gives the recommended solution for T2C (Groenewegen 2020a).

than the SMC ones (this is so when γ is negative, and fitting only the SMC and LMC data points gives $\gamma = -0.04$) but it would imply that the ZP for the MW Cepheids is too faint by $(-0.75 - +0.08) \cdot -0.29 \approx 0.24$ mag. Further study is required, especially on the MW sample, and parallaxes from *Gaia* DR4 will be crucial in this regard. Additionally, the difference between the bolometric magnitude and the magnitude in any photometric band involves a bolometric correction that should depend on wavelength and makes a direct comparison of the γ terms less evident.
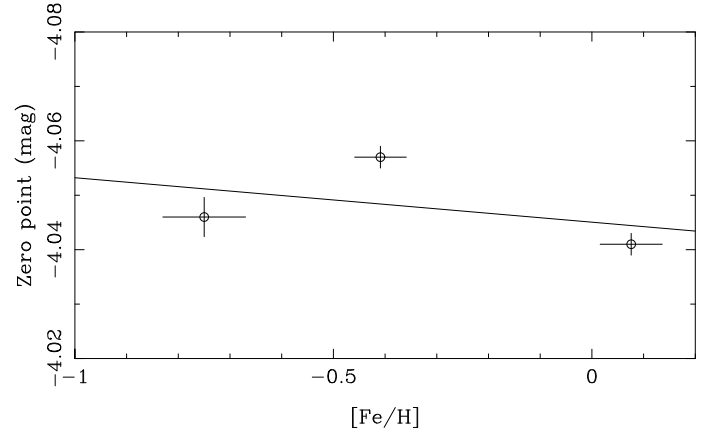
Fig. 6. Zero point at 10 days of the PL-relation for SMC, LMC, and MW. The line is a linear fit with a slope (0.0082 ± 0.0076) mag dex^{-1} which is not significant.

4.5. Period-radius relation

Figure 7 shows the PR relation. The relation for the LMC is:

$$\log R = (0.6966 \pm 0.0043) \log P + (1.1194 \pm 0.0052), \tag{9}$$

with an rms of 0.017 dex and using 138 stars (removing 4 outliers), and then for the SMC

$$\log R = (0.697 \pm 0.013) \log P + (1.134 \pm 0.017), \tag{10}$$

with an rms of 0.027 dex and using 76 stars (removing 1 outlier). Figure 7 also shows the PR relation for MW CCs from G20. The slope derived there was 0.721 ± 0.013 with a ZP of 1.083 ± 0.012. Refitting the data in G20 restricting the metallicity to $0.0 \leq$ [Fe/H] $<+0.2$ gives:

$$\log R = (0.668 \pm 0.020) \log P + (1.143 \pm 0.017), \tag{11}$$
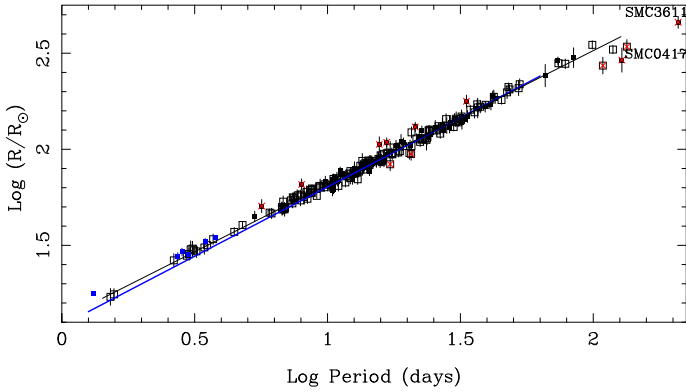
Fig. 7. Period-radius relation. LMC objects are plotted as open squares, SMC objects are filled squares. Blue symbols indicate the six CCs in EBs. Outliers removed from the fit are marked by a red cross and some are identified. The black line indicates the best fit (excluding the outliers) to the complete MC sample. Fits to the LMC and SMC stars separately are given in the text. The blue line gives the PR relation for MW CCs from G20.

with an rms of 0.069 dex and using 190 stars. The slopes are consistent with each other and at $P = 10$ d the radii in MW, LMC, and SMC CCs are identical to within the error bars.
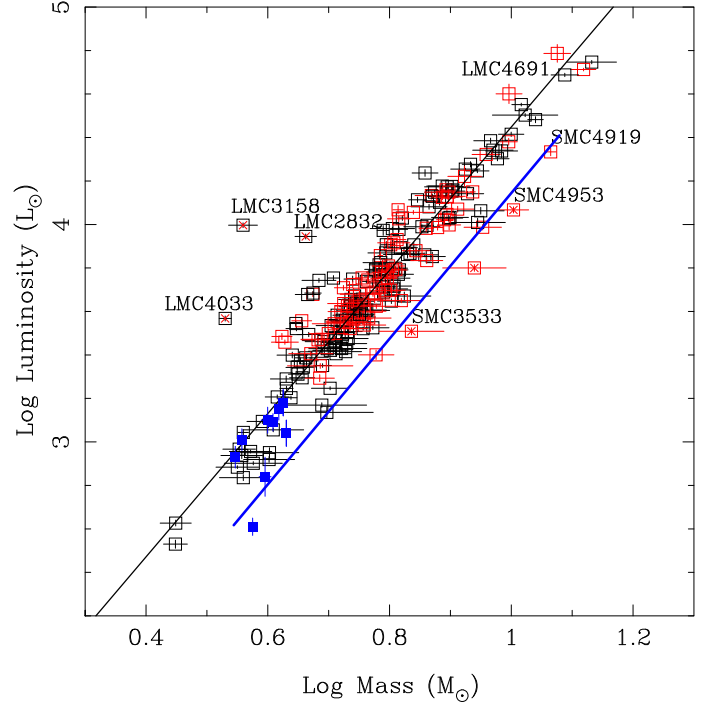
4.6. The mass-luminosity relation

Figure 8 shows the relation between mass and luminosity. The best fit is:

$$\log L = (3.193 \pm 0.060)\log M + (1.237 \pm 0.048) \qquad (12)$$

based on 208 stars and an rms of 0.12 dex, and lies approximately 0.3 dex above the canonical ML relation from Bono et al. (2000a) for Helium abundance $Y = 0.255$ and metallicity $Z = 0.008$. A few stars scatter clearly above the relation. The few stars that scatter below the best-fit relation are consistent with the canonical ML relation. The best-fit relation is the intermediate between the case B (+0.2 dex w.r.t. the canonical relation) and case C (+0.4 dex) ML relations adopted in Marconi et al. (2020).

4.7. Comparing stellar parameters

The determination of the photometric effective temperature allows one to compare it to the spectroscopic temperature determined in the literature. In addition, via the derived luminosity, and estimated mass, it is possible to compare the gravity to that derived by spectroscopy. The values for the spectroscopic effective temperature and gravity come from the papers that contribute a large fraction of the stars in the sample (Romaniello et al. 2008, 2022; Lemasle et al. 2017). In addition, spectroscopicly derived parameters from the APOGEE survey have been considered (Sprague et al. 2022), as well as the values derived from the LC fitting in Ragosta et al. (2019) and Marconi et al. (2017). The adopted values for temperature and gravity are listed in Cols. 6 and 7 of Table 1. When data from multiple references were available the order of preferences was Romaniello et al. (2022, 2008), Lemasle et al. (2017), Sprague et al. (2022), and Marconi et al. (2017) or Ragosta et al. (2019). Results from GDR3 were not considered in the end. The results from the GSP_Spec analysis (Recio-Blanco et al. 2023) were inspected but only one, respectively two, had an entry from the so called Matisse-Gauguin and ANN pipeline when

Fig. 8. Mass-luminosity relation. Objects in the LMC are plotted as black, those in the SMC as red open squares. Stars outside the bulk of objects are identified. Objects in blue are the known CCs and their companions in EBs. The blue line indicates the canonical ML relation from Bono et al. (2000a) for $Y = 0.255$ and $Z = 0.008$. For $Z = 0.004$ the line would be at higher luminosities by about 0.1 dex. The black line indicates a fit to the LMC stars minus the outliers (see Eq. (12)) and lies almost exactly +0.3 dex above the canonical ML relation.

selecting '000000' for the first six values in the `flags_gspspec` and `flags_gspspec_ann` flags.

Figure 9 shows the comparison of the photometric and literature temperatures. On average the spectroscopic temperatures seem to be slightly larger, although there is large scatter. The median offset is $+91 \pm 330$ K. The effective temperature changes over the pulsation cycle so an exact agreement is in fact not expected. The spectra taken from the works dedicated to determining the metallicity (and $T_{\rm eff}$ and $\log g$ in the process, Romaniello et al. 2008, 2022; Lemasle et al. 2017) of CCs typically try to avoid the phases where shocks play a role the objects. On the other hand the APOGEE data were taken at random phases while the photometric temperatures was derived from the SED that was constructed to be as much as representative of mean light as possible.

Figure 10 shows the same for the $\log g$ values determined in the literature. The overall median offset is -0.70 ± 0.36 dex, but it strongly depends on the source. The $\log g$ values derived from the pulsation models are in very good agreement with the values determined in the present paper, the values from APOGEE are larger (median offset $+0.58 \pm 0.46$ dex), while those derived from dedicated HR spectroscopy are significantly smaller (median offset -0.80 ± 0.21). A similar plot for the FWG is shown in the Appendix (Fig. D.4).

The differences between the spectroscopic and photometric effective temperature are relatively small, but the spectroscopically determined gravity (and the FWG) from Romaniello et al. (2008, 2022) and Lemasle et al. (2017) are systematically and significantly smaller than that derived from L, $T_{\rm eff}$, and stellar mass. Like the effective temperature the gravity also changes
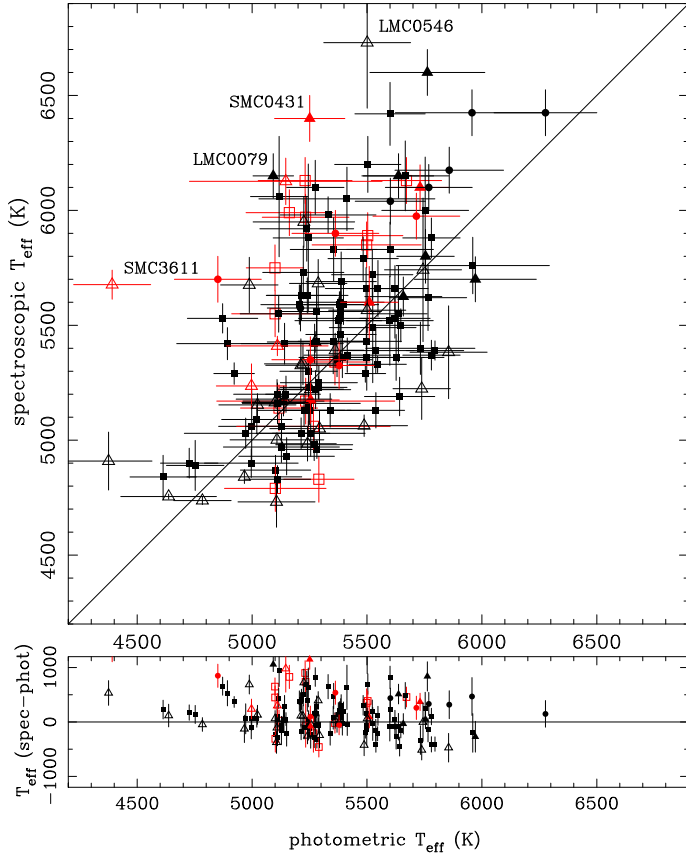
Fig. 9. Comparison between the effective temperatures determined from the SED fitting and in the literature. Objects in the LMC are plotted in black and objects in the SMC in red. The one-to-one line is indicated. Stars where the absolute difference is larger than 1000 K are identified. Objects from reference 1 and 2 (see the note to Table 1) are plotted as filled squares, from reference 3 as open squares, from reference 4 as filled triangles, from reference 5 as open triangles, and from reference 6 as filled circles. In the lower panel, the difference between literature and photometric temperature is plotted.

over the pulsation cycle. There is a change in radius, but there is also a dynamical term. What is thus determined from HR spectroscopy is the effective gravity:

$$g_{\mathrm{eff}} = \frac{G\,M}{R(t)^2} + \frac{\partial^2 R}{\partial t^2} = \frac{G\,M}{R(t)^2} - p\,\frac{\partial V_{\mathrm{r}}(t)}{\partial t}, \tag{13}$$

where M is the mass of the CC, $R(t)$ is the radius as a function of time (or pulsation phase), p is the projection factor (see Nardetto et al. 2004 and references therein) and $V_{\mathrm{r}}(t)$ is the radial velocity at the time t.

Recently, da Silva et al. (2022) presented time series of HR spectroscopy for 20 calibrating MW CCs and the analysis of these spectra in terms of radial velocities, metallicities, micro turbulent velocities, gravities and effective temperatures (see their Appendix B). This unique dataset also allows to study the effect of the effective gravity. The dynamical term $\frac{\partial V_{\mathrm{r}}(t)}{\partial t}$ at each phase point ϕ_i was approximated as $\frac{V_{\mathrm{r}}(\phi_{i+1}) - V_{\mathrm{r}}(\phi_{i-1})}{\Delta t}$ and a typical p factor of 1.25 was adopted.

The effective gravity is calculated as $\log g_{\mathrm{eff}} = 10^{\log g_{\mathrm{mean}}} +$ (dynamical term), where g_{mean} is the weighted mean gravity over all available phase points (recalculated in the present paper and identical to the values in Table 6 of da Silva et al. 2022). This ignores the variation in radius with phase but this effect is
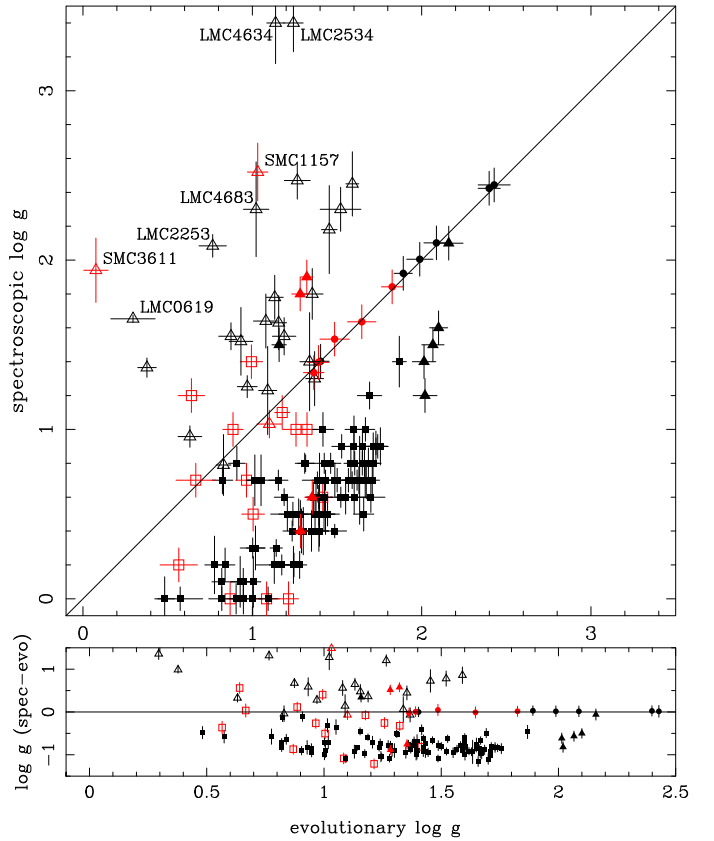
Fig. 10. Comparison between the $\log g$ determined in the literature, and the evolutionary value as determined from L and T_{eff} from the SED fitting and the stellar mass based on various methods (see Appendix B). The one-to-one line is indicated. Stars outside the bulk of objects are identified. Symbols as in Fig. 9.

smaller than the dynamical term (Appendix C). Figure 11 shows the result for δ Cep. The figure is ordered in such a way that the dynamical term appears below the RV curve and the calculated effective gravity appears below the observed gravity. Contrary to the convention in da Silva et al. (2022) phase 0 is taken at maximum light. Plots for some of the stars with the best phase coverage are shown in Appendix D (Figs. D.5–D.8). Overall there is reasonable to good correspondence between the effective gravity and the observed gravity, and the expected rise in gravity due to the dynamical terms occurs at the correct phase. The results show that if observations are taken at phases that avoid the sharp rise in radial velocity the effective temperature and gravity will be systematically lower than the average over the light curve. However, the effect should be a few 0.1 dex, and cannot explain the large difference between the spectroscopic and evolutionary gravity noted in Fig. 10. The behaviour of the effective gravity is also confirmed by a theoretical model, see Appendix C. It is beyond the scope of the present paper, but the analysis of time series data, as presented in da Silva et al. (2022), allows one to put constrains or derive the p-factor for individual stars, as the dynamical term is proportional to p and the effective gravity should match the observed gravity.

4.8. FWG-period and the FWGLR

Figure 12 shows the relation between the FWG and the pulsation period based on the analysis in the present paper as well as on
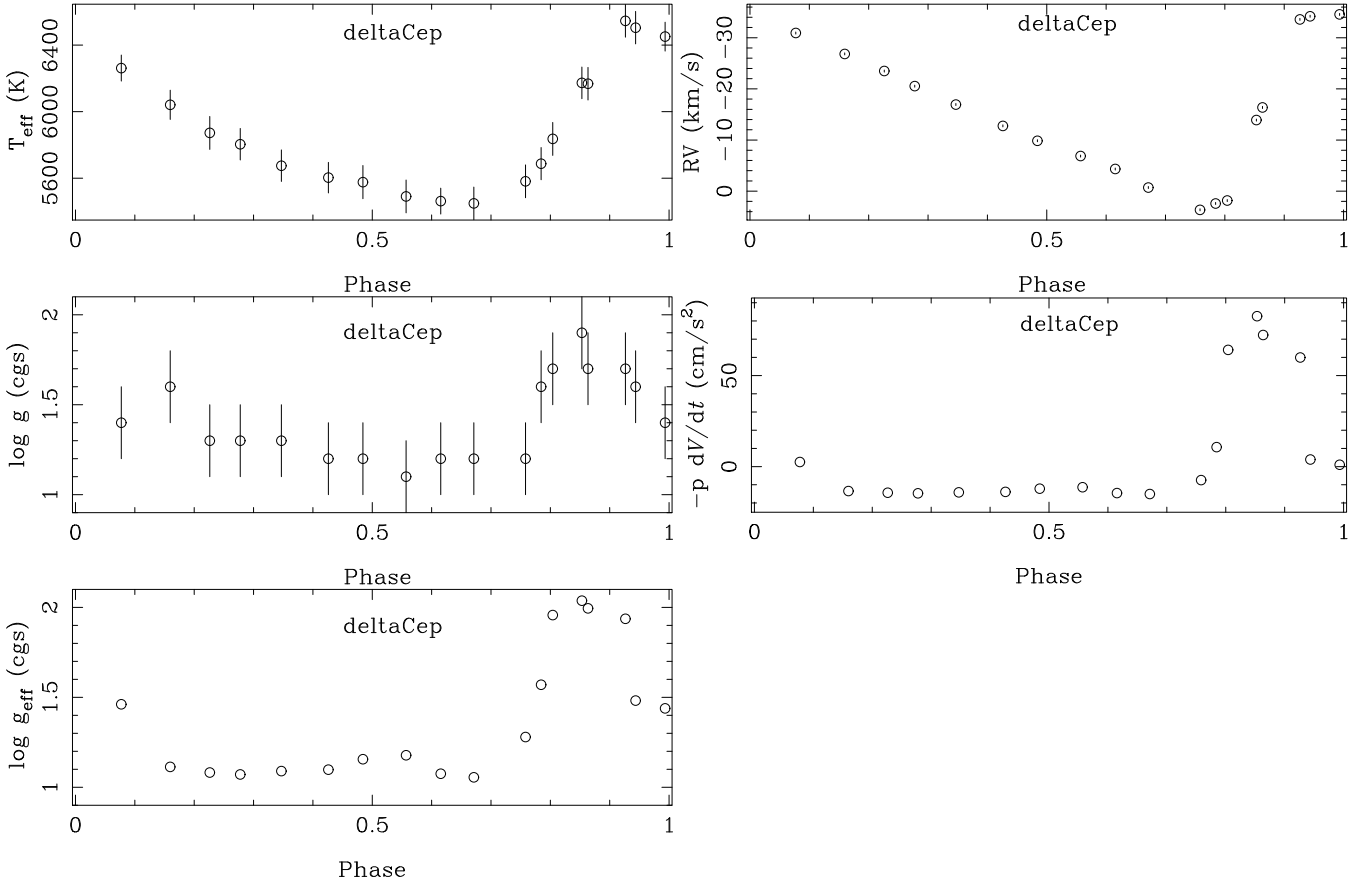
Fig. 11. Time series of effective temperature, radial velocity and gravity for δ Cep from da Silva et al. (2022). Calculated in the presented paper are the dynamical term and the effective gravity based on the mean gravity and the dynamical term. The ordinate for the effective gravity is set to that of the observed gravity.
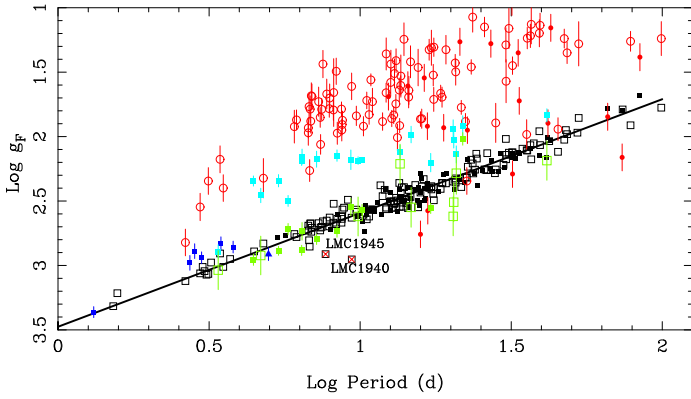
Fig. 12. FWG versus $\log P$. Black points indicate the FWGs derived from L and $T_{\rm eff}$ (from the SED fitting) and stellar mass in the present paper. Black open squares are LMC objects, filled squares indicate SMC objects. Blue symbols indicate the CCs (filled squares) and one T2C (filled triangle) in EB systems. The black line is a fit to the black points, minus the two marked outliers. The red circles indicate FWGs from HR spectroscopy (open circles indicate LMC, filled circles indicate SMC), Light blue filled squares indicate FWGs of 20 MC CCs from da Silva et al. (2022), while the green points indicate the FWGs for the same 20 objects from Luck (2018; open squares indicate that only one spectrum is available in Luck 2018, filled squares indicate that five or more spectra are available).
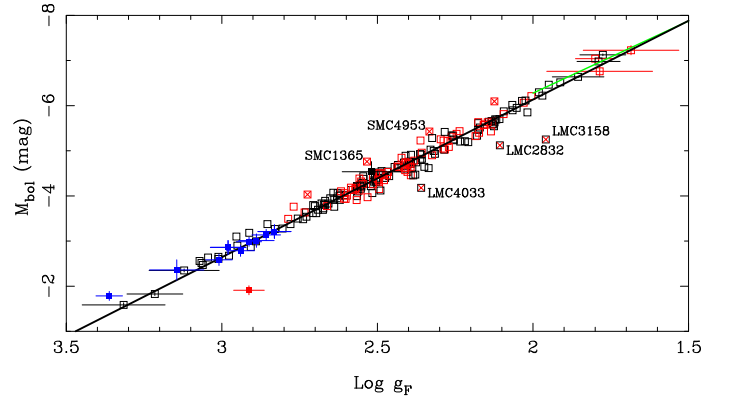
Fig. 13. FWGLR: LMC and SMC objects are identified by black and red open squares. To avoid cluttering the plot, representative error bars are plotted for the smallest and largest values of $\log g_{\rm F}$ only. Some outliers are marked, and stars excluded from the fit are marked by a red cross. Blue filled squares indicate the six EB CCs and their companions, the filled red square indicates the T2C in the LMC-T2CEP-098 system and the filled black square its companion. The black line gives the best fit to the objects (Eq. (16)). The green line at small FWGs is the fit to LMC BSGs (Urbaneja et al. 2017; Bresolin et al. 2022).

$$\log g_{\rm F} = (-0.856 \pm 0.016) \, \log P + (3.442 \pm 0.019) \quad (14)$$

the available HR observations for the sample and two identical samples of MW CCs. The best fit to the LMC objects is:

with an rms of 0.057 dex, and is indistinguishable from the best fit to the SMC objects:

$$\log g_{\rm F} = (-0.854 \pm 0.033) \ \log P + (3.442 \pm 0.042) \qquad (15)$$

with an rms of 0.062 dex. The preferred solution combines the SMC and LMC objects as follows:

$$\log g_{\rm F} = (-0.853 \pm 0.014) \ \log P + (3.442 \pm 0.017) \qquad (16)$$

with an rms of 0.059 dex using 212 stars. This relation is in good agreement both with the theoretical prediction $\log g_{\rm F} = (-0.834 \pm 0.011) \ \log P + (3.402 \pm 0.011)$, derived in Groenewegen (2020b) based on the models in Anderson et al. (2016) and the relation $\log g_{\rm F} = (-0.80 \pm 0.03) \ \log P + (3.43 \pm 0.03)$ derived for MW CCs (Groenewegen 2020b).

Of interest are the location of all the coloured points in this plot. The blue points indicate the CCs and one T2C in EBs and these agree well with the observed relation. That some appear to be slightly above the relation could be related to an overestimate of the effective temperature, as argued before. The red circles indicate the objects from the sample where a FWG is available from HR spectroscopy. Almost all lie clearly above the relation, and those that do appear to be on a line parallel to the derived relation with on offset of about 0.8 dex (also see Fig. D.4). To investigate this further we again used the data from da Silva et al. (2022) on 20 calibrating MW CCs. These points are the light blue squares[8]. Except for the shortest period value (R TrA at $P = 3.4$ days), which agrees well with the mean relation all others form a sequence that lies above and is inclined to the mean relation. All these 20 CCs also have (in part multi-epoch) HR spectroscopy data that is analysed in Luck (2018), which was the main source of data used in our previous study on MW Cepheids (Groenewegen 2020b). These points are the green squares and those fit Eq. (16) very well. If we demand that the absolute difference between the observed FWG and that predicted by Eq. (16) is less than $\left(\delta \cdot \sqrt{0.059^2 + \sigma_{\rm FWG}^2} \right)$ with $\sigma_{\rm FWG}$ the observed error in the FWG than all 20 objects from Luck (2018) obey this relation for $\delta = 1.5$. For this value of δ only 4 out of the same 20 objects obey this relation using the FWGs from da Silva et al. (2022) – and even these four stars all lie above the relation – and only 9[9] out of 104 stars using the FWGs as derived from HR spectroscopy in the MCs. It is beyond the scope of the present paper to investigate this further (see also the discussion and appendix in Groenewegen 2020b, where a similar effect was noticed). Nevertheless, Fig. D.9 shows the comparison between temperature, gravity, and the differential between Luck (2018) and da Silva et al. (2022) for the same 20 objects. Most interesting is the result that there is a correlation between the two data sets. When for an object $T_{\rm eff}$ is larger in Luck (2018) then in da Silva et al. (2022), then also the gravity is larger.

Figure 13 shows the FWGLR. Using a least-squares fit taking into account errors in both axes gives the following fit to the LMC objects:

$$M_{\rm bol} = (3.479 \pm 0.032)(\log g_{\rm F} - 2.5) - (4.390 \pm 0.010), \qquad (17)$$

with an rms of 0.16, and a fit to the SMC CCs of:

$$M_{\rm bol} = (3.577 \pm 0.097)(\log g_{\rm F} - 2.5) - (4.390 \pm 0.021), \qquad (18)$$

with an rms of 0.12. The combined fit is the preferred solution and is expressed as:

$$M_{\rm bol} = (3.492 \pm 0.028)(\log g_{\rm F} - 2.5) - (4.388 \pm 0.009), \qquad (19)$$

---

[8] FF Aql is an overtone pulsator and the star is plotted at its fundamentalised period of 6.401 days.

[9] These are LMC 0079, 0461, 2019, 2832, and 3724, and SMC 0431, 0574, 0921, and 4444.

with an rms of 0.12 mag using 207 objects. Blue filled squares in the plot indicate the six EB CCs and their companions, the filled red square indicates the T2C in the LMC-T2CEP-098 system and the filled black square its companion. Except for the T2C itself, the CCs, and the companions agree very well with Eq. (19). Where there is overlap at small FWGs, there is also good agreement with the FWGLR derived for BSGs in the LMC (Urbaneja et al. 2017; Bresolin et al. 2022).

This demonstrates the power of the FWGLR as the BSGs have masses in the range 12–40 $M_\odot$ (Fig. 5 in Urbaneja et al. 2017), while the Cepheids in the present sample have lower masses that are estimated to be in the range 2.8–13.5 $M_\odot$ (median of about 6 $M_\odot$). Using evolutionary tracks Kudritzki et al. (2020) demonstrated that, what they named an "extended," FWGLR is expected over 17 magnitudes in $M_{\rm bol}$ (with a scatter of 0.17 mag below $M_{\rm bol} = -3.0$ mag) and for masses in the range 0.8–40 $M_\odot$, which they verfied using a sample of RGB stars with a typical mass of 1.1 $M_\odot$.

5. Discussion and summary

This paper is a follow-up of G20 and Groenewegen (2020b), where the SEDs of 477 MW Cepheids were fitted. All stars had metallicities based on HR spectroscopy from the literature. Excluding non-CCs and overtone pulsators the PL, the PR and other relations were typically based on about 370 FM CCs. Some of the relations have been redetermined in the present paper using a restricted range in metallicity to have a sample of MW CCs with near solar metallicities and these relations are typically based on 190 CCs.

The present study covers 142 LMC and 77 SMC FM CCs. All known (FM) CCs in the MCs with metallicities based on HR spectroscopy are included and those constitute about half of the sample. Other CCs are included because they were studied otherwise (for example a Baade-Wesselink analyses was conducted) or may be of interest in future work (ongoing spectroscopic or *HST* observations). The advantage of the current sample compared to the MW sample is that the reddening is better established and, in particular, the distance is well known for the MCs. This means that the PL, PR, and other relations have better determined slopes and smaller residuals compared to the MW relations.

One interesting result is that the zero point of the bolometric PL relation (when fixing the slope to that of the LMC) does not seem to depend on metallicity, contrary to the recent result that in photometric filters covering a large range in wavelength there is a significant metallicity terms that is essentially constant with wavelength (Breuval et al. 2022 and references therein). A new study of MW CCs with improved distances from *Gaia* DR4 could strengthen this conclusion.

The power of the FWG is again demonstrated. Both the relation of the FWG with period and with luminosity are very tight. The relation based on the present analysis (gravity derived from the radius, that follows from $T_{\rm eff}$ and L, and the stellar mass as derived from several relations) is in excellent agreement with theory and (where it overlaps) with the relation derived for BSGs. However, a large fraction of the stars in the sample for which gravities and effective temperatures have been derived from HR spectroscopy show gravities and FWGs that are smaller than expected by about 0.8 dex. For the MW sample two recent studies that both analyse time series of HR spectra show strikingly different results in this respect. The FWGs based on da Silva et al. (2022) lie mostly above the expected FWG-period relation (but less so than for the MCs), while the FWGs

based on Luck (2018) for the identical sample of 20 stars are in very good agreement with this relation. Its is beyond this paper to try to resolve this discrepancy as it must be related to the details of the spectroscopic analysis approach. Of note is that the effective temperature and gravity differences between da Silva et al. (2022) and Luck (2018) appear correlated. Since gravity, effective temperature, micro turbulent velocity, and metallicity are determined simultaneously in a spectroscopic analysis it is of interest to investigate whether these correlations also lead to different metallicity estimates. This appears not to be the case (bottom right panel in Fig. D.9). Restricting oneself to the 11 stars, where there are 5 or more available spectra per star in Luck (2018) the difference in metallicity between Luck (2018) and da Silva et al. (2022) is 0.00 ± 0.05 dex. Thus, at least at solar metallicities the (correlated) differences between temperature and gravity determinations do not lead to differences in metallicity. It remains to be seen whether this is also the case at lower metallicities where the differences in gravity are much larger.

References

Anderson, R. I., Saio, H., Ekström, S., Georgy, C., & Meynet, G. 2016, A&A, 591, A8
Bianchi, L., Shiao, B., & Thilker, D. 2017, ApJS, 230, 24
Bono, G., Caputo, F., Cassisi, S., et al. 2000a, ApJ, 543, 955
Bono, G., Castellani, V., & Marconi, M. 2000b, ApJ, 529, 293
Breitfelder, J., Mérand, A., Kervella, P., et al. 2016, A&A, 587, A117
Bresolin, F., Kudritzki, R.-P., & Urbaneja, M. A. 2022, ApJ, 940, 32
Breuval, L., Riess, A. G., Kervella, P., Anderson, R. I., & Romaniello, M. 2022, ApJ, 939, 89
Castelli, F., & Kurucz, R. L. 2003, in Modelling of Stellar Atmospheres, 210, eds. N. Piskunov, W. W. Weiss, & D. F. Gray, A20
Chown, A. H., Scowcroft, V., & Wuyts, S. 2021, MNRAS, 500, 817
Cioni, M.-R. L., Clementini, G., Girardi, L., et al. 2011, A&A, 527, A116
Cutri, R. M., et al. 2014, VizieR Online Data Catalog: 2328, 0
da Silva, R., Crestani, J., Bono, G., et al. 2022, A&A, 661, A104
de Ruiter, H. R., & Lub, J. 1986, A&AS, 63, 59
De Somma, G., Marconi, M., Cassisi, S., et al. 2021, MNRAS, 508, 1473
Eggen, O. J. 1977, ApJS, 34, 33
Gaia Collaboration (Prusti, T., et al.) 2016, A&A, 595, A1
Gaia Collaboration (Vallenari, A., et al.) 2023, A&A, 674, A1
Gallenne, A., Kervella, P., & Mérand, A. 2012, A&A, 538, A24
Gallenne, A., Mérand, A., Kervella, P., et al. 2013, A&A, 558, A140
Gallenne, A., Kervella, P., Mérand, A., et al. 2017, A&A, 608, A18
Graczyk, D., Pietrzyński, G., Thompson, I. B., et al. 2020, ApJ, 904, 13
Groenewegen, M. A. T. 2004, A&A, 425, 595
Groenewegen, M. A. T. 2012, A&A, 543, A36
Groenewegen, M. A. T. 2013, A&A, 550, A70
Groenewegen, M. A. T. 2018, A&A, 619, A8
Groenewegen, M. A. T. 2020a, A&A, 635, A33
Groenewegen, M. A. T. 2020b, A&A, 640, A113
Groenewegen, M. A. T. 2022, A&A, 659, A145
Groenewegen, M. A. T., & Jurkovic, M. I. 2017, A&A, 604, A29
Groenewegen, M. A. T., Nanni, A., Cioni, M. R. L., et al. 2020, A&A, 636, A48
Gustafsson, B., Edvardsson, B., Eriksson, K., et al. 2008, A&A, 486, 951
Ita, Y., Onaka, T., Tanabé, T., et al. 2010, PASJ, 62, 273
Ivezić, Ž., Nenkova, M., & Elitzur, M. 1999, DUSTY: Radiation transport in a dusty environment, Astrophysics Source Code Library
Kato, D., Ita, Y., Onaka, T., et al. 2012, AJ, 144, 179
Kervella, P., Mérand, A., Perrin, G., & Coudé du Foresto, V. 2006, A&A, 448, 623
Kim, D.-W., Protopapas, P., Bailer-Jones, C. A. L., et al. 2014, A&A, 566, A43
Kudritzki, R. P., Bresolin, F., & Przybilla, N. 2003, ApJ, 582, L83
Kudritzki, R.-P., Urbaneja, M. A., Bresolin, F., et al. 2008, ApJ, 681, 269
Kudritzki, R. P., Castro, N., Urbaneja, M. A., et al. 2016, ApJ, 829, 70
Kudritzki, R.-P., Urbaneja, M. A., & Rix, H.-W. 2020, ApJ, 890, 28
Lemasle, B., Groenewegen, M. A. T., Grebel, E. K., et al. 2017, A&A, 608, A85
Lindegren, L., Hernández, J., Bombrun, A., et al. 2018, A&A, 616, A2
Lindegren, L., Bastian, U., Biermann, M., et al. 2021, A&A, 649, A4
Luck, R. E. 2018, AJ, 156, 171
Macri, L. M., Ngeow, C.-C., Kanbur, S. M., Mahzooni, S., & Smitka, M. T. 2015, AJ, 149, 117
Madore, B. F. 1975, ApJS, 29, 219
Madore, B. F. 1982, ApJ, 253, 575
Marconi, M., Molinaro, R., Ripepi, V., Musella, I., & Brocato, E. 2013, MNRAS, 428, 2185
Marconi, M., Molinaro, R., Ripepi, V., et al. 2017, MNRAS, 466, 3206
Marconi, M., De Somma, G., Ripepi, V., et al. 2020, ApJ, 898, L7
Martin, W. L., & Warren, P. R. 1979, South Afr. Astron. Observatory Circ., 1, 98
Mérand, A., Kervella, P., Coudé du Foresto, V., et al. 2006, A&A, 453, 155
Mérand, A., Kervella, P., Breitfelder, J., et al. 2015, A&A, 584, A80
Molinaro, R., Ripepi, V., Marconi, M., et al. 2012, ApJ, 748, 69
Musella, I., Marconi, M., Stetson, P. B., et al. 2016, MNRAS, 457, 3084
Nardetto, N., Fokin, A., Mourard, D., et al. 2004, A&A, 428, 131
Nardetto, N., Mérand, A., Mourard, D., et al. 2016, A&A, 593, A45
Onken, C. A., Wolf, C., Bessell, M. S., et al. 2019, PASA, 36, e033
Pel, J. W., van Genderen, A. M., & Lub, J. 1981, A&A, 99, A1
Persson, S. E., Madore, B. F., Krzemiński, W., et al. 2004, AJ, 128, 2239
Pietrzyński, G., Graczyk, D., Gallenne, A., et al. 2019, Nature, 567, 200
Pilecki, B., Gieren, W., Pietrzyński, G., et al. 2018, ApJ, 862, 43
Ragosta, F., Marconi, M., Molinaro, R., et al. 2019, MNRAS, 490, 4975
Recio-Blanco, A., de Laverny, P., Palicio, P. A., et al. 2023, A&A, 674, A29
Riess, A. G., Casertano, S., Yuan, W., et al. 2018, ApJ, 861, 126
Riess, A. G., Casertano, S., Yuan, W., Macri, L. M., & Scolnic, D. 2019, ApJ, 876, 85
Riess, A. G., Casertano, S., Yuan, W., et al. 2021, ApJ, 908, L6
Riess, A. G., Yuan, W., Macri, L. M., et al. 2022, ApJ, 934, L7
Ripepi, V., Marconi, M., Moretti, M. I., et al. 2016, ApJS, 224, 21
Ripepi, V., Cioni, M.-R. L., Moretti, M. I., et al. 2017, MNRAS, 472, 808
Ripepi, V., Molinaro, R., Musella, I., et al. 2019, A&A, 625, A14
Ripepi, V., Chemin, L., Molinaro, R., et al. 2022, MNRAS, 512, 563
Ripepi, V., Clementini, G., Molinaro, R., et al. 2023, A&A 674, A17
Romaniello, M., Primas, F., Mottini, M., et al. 2008, A&A, 488, 731
Romaniello, M., Riess, A., Mancino, S., et al. 2022, A&A, 658, A29
Sebo, K. M., Rawson, D., Mould, J., et al. 2002, ApJS, 142, 71
Skowron, D. M., Skowron, J., Udalski, A., et al. 2021, ApJS, 252, 23
Soszyński, I., Udalski, A., Szymański, M. K., et al. 2017, Acta Astron., 67, 103
Sprague, D., Culhane, C., Kounkel, M., et al. 2022, AJ, 163, 152
Storm, J., Gieren, W., Fouqué, P., et al. 2011, A&A, 534, A95
Trahin, B. 2019, PhD thesis, Université PSL, Observatoire de Paris, France
Trahin, B., Breuval, L., Kervella, P., et al. 2021, A&A, 656, A102
Trundle, C., Dufton, P. L., Hunter, I., et al. 2007, A&A, 471, 62
Udalski, A., Szymanski, M., Kubiak, M., et al. 1998, Acta Astron., 48, 147
Udalski, A., Szymanski, M., Kubiak, M., et al. 2000, Acta Astron., 50, 307
Ulaczyk, K., Szymański, M. K., Udalski, A., et al. 2012, Acta Astron., 62, 247
Ulaczyk, K., Szymański, M. K., Udalski, A., et al. 2013, Acta Astron., 63, 159
Urbaneja, M. A., Kudritzki, R. P., Gieren, W., et al. 2017, AJ, 154, 102
van der Marel, R. P., & Kallivayalil, N. 2014, ApJ, 781, 121
van Genderen, A. M. 1981, A&A, 101, 289
van Genderen, A. M. 1983, A&AS, 52, 423
van Genderen, A. M., & Nitihardjo, G. H. 1989, A&A, 221, 230
Vasilyev, V., Ludwig, H. G., Freytag, B., Lemasle, B., & Marconi, M. 2017, A&A, 606, A140
Vasilyev, V., Ludwig, H. G., Freytag, B., Lemasle, B., & Marconi, M. 2018, A&A, 611, A19
Walraven, T., & Walraven, J. H. 1960, Bull. Astron. Inst. Netherlands, 15, 67

Appendix A: Walraven photometry

van Genderen (1983) published Walraven data taken between 1971 and 1978 of CCs in the MCs at the Leiden southern station in Hartebeespoordam in South Africa. The telescope and photometer were moved to La Silla observatory at the end of 1978 where the data taking continued from January 1979 onwards. The move was also used to make several improvements to the system (Pel et al. 1981; de Ruiter & Lub 1986).

Table A.1 collects these, as of yet, largely unpublished photometry for CCs (some initial results were presented in Pel et al. 1981 and van Genderen & Nitihardjo 1989 for HDE 270100). The HV number, the Heliocentric Julian date (HJD) of the observations, and the V, $V - B$, $B - U$, $U - W$, and $B - L$ colours on the Walraven system are listed[10]. The last column lists a quality flag, that ranges between 0 and 9 (in fact, it can be a '*' for extremely poor observations, but these have been filtered out). However, photon statistics also play a role for fainter objects. Light curves were inspected and fitted to determine what typical rms values can be achieved as a function of the quality flags for the magnitude range of these Cepheids. In the end an uncertainty of 0.015 is adopted for quality flags 0-5, and 0.019, and 0.037 in $\log I$ for quality flags 6 and 7, respectively. Points with a quality flags 8 and 9 are excluded from the fitting of the light curves.

For stars already observed by van Genderen (1983) the new data were added to the published data, after applying the following corrections to the data in van Genderen (1983) that reflect the slightly different photometric system and set-up between the 1971-1978 and the later observations. Referring to these as the "70" and the "80" system, respectively, these corrections are:

$$V80 = V70 + 0.0417\ VB70 - 0.0007\ (\text{std.dev.} = 0.0055)$$
$$B80 = B70 - 0.0494\ VB70 - 0.0003\ (\text{std.dev.} = 0.0067)$$
$$L80 = L70 - 0.0569\ BL70 - 0.0007\ (\text{std.dev.} = 0.0075)$$
$$U80 = U70 - 0.0151\ BU70 - 0.0007\ (\text{std.dev.} = 0.0077)$$
$$W80 = W70 - 0.2085\ UW70 + 0.0007\ (\text{std.dev.} = 0.0128)$$

(A.1)

which are based on a set of about 1000 stars measured at both sites. The quality flag is not given by van Genderen (1983) and an error of 0.015 has been adopted in VBL, 0.02 in U, and 0.025 in W. Points marked by a ':' in that paper were excluded.

The procedure in MoD is to use photometric zero points that are determined independently based on a model of Vega using the respective filter curves (see Groenewegen 2012 for details, and the link to the latest available version of MoD given before). The calibration constants derived in this way are $-11.184, -10.923, -10.831, -10.808$, and -10.684 (in units of $\log$ ergs/cm^2/s/Å) in VBLUW, respectively, and that differ on average by 0.008 from the empirically determined values of $-11.176, -10.914, -10.818, -10.800$, and -10.681 (J. Lub's unpublished determination in 2019), that supersede the values of $-11.172, -10.910, -10.818, -10.793$, and -10.673 as published in de Ruiter & Lub (1986). Although not used in this paper the updated conversions to Johnson V_J and $(B - V)_J$ are

$$V_J = 6.8819 - 2.5 \cdot (V80 + 0.0280\ (V80 - B80))$$
$$(\text{std.dev.} = 0.017),$$
$$(B - V)_J = 2.528 \cdot (B80 - V80) - 0.817 \cdot (B80 - V80)^2 +$$
$$0.336 \cdot (B80 - V80)^3 - 0.0133\ (\text{std.dev.} = 0.016).$$

(A.2)

---

[10] It is recalled that Walraven photometry is given on a log intensity (I) scale, not on a magnitude scale.
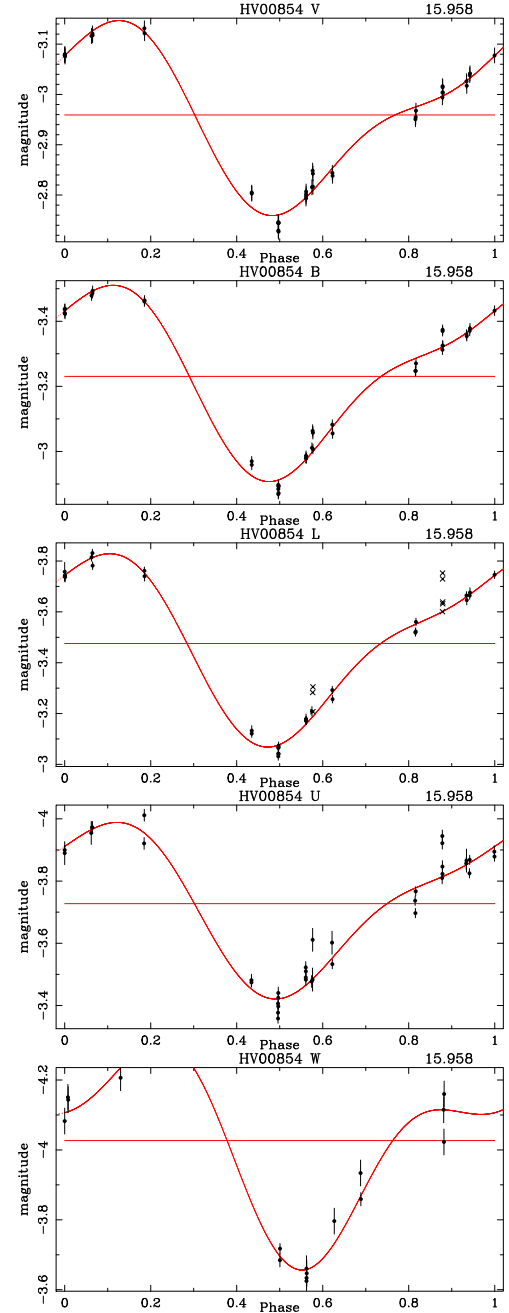
Fig. A.1. Example of the fit to the light curves for HV 854. The name filter is listed at the top, as well as the period to the right at the top. The red lines indicate the model fit and the mean value. Crosses indicate points that were flagged as outliers and excluded from the fit.

The data were fitted with the code described and used in Groenewegen (2004); Groenewegen et al. (2020); Groenewegen (2022) tailored to the Walraven data. The light curves are analysed using a fixed period, fitting for the mean and the amplitude. Depending on the number of available data points the first harmonic period was added in the fit, solving for its amplitude as well. The mean and total amplitude are reported in Table A.2. To the error in the mean a value of 0.015 is added in quadrature. The first entries (HV 824 - 5655) are the stars with new observations, the latter part (HDE 270100 - HV 12815) are the stars from van Genderen (1983) (and van Genderen & Nitihardjo 1989 for HDE 270100) with any new data added in the analysis. An example of the fit to the light curves is shown in Fig. A.1.

Table A.1. Walraven photometry (first entries).

HV	HJD	V	$V - B$	$B - U$	$U - W$	$B - L$	quality flag
824	44888.71073	-2.1162	0.3236	0.5142	0.3871	0.2958	23567
824	44888.71293	-2.1132	0.3251	0.5184	0.3475	0.2882	31455
824	44888.72042	-2.1097	0.3235	0.5253	0.4162	0.2944	22327
824	44888.74559	-2.1149	0.3195	0.4963	0.2780	0.2896	23465
824	44889.66239	-2.1098	0.3336	0.5410	0.2926	0.2862	23446
824	44889.66896	-2.1111	0.3293	0.5147	0.3777	0.3058	23557
824	44923.60442	-2.3975	0.5251	0.5336	0.3109	0.4165	35567
824	44923.60992	-2.3974	0.5199	0.5632	0.3065	0.4213	45558
829	44889.55646	-2.0115	0.3132	0.5072	0.4083	0.2822	24455
829	44889.56281	-2.0095	0.3140	0.5197	0.3526	0.2860	22456
829	44889.58245	-2.0132	0.3208	0.5008	0.3641	0.2753	23546
829	44889.59266	-1.9977	0.3145	0.4774	0.3383	0.2802	23455
829	44923.62044	-1.9865	0.3854	0.5519	0.4616	0.3439	23357
829	44923.62577	-1.9864	0.3862	0.5640	0.4396	0.3506	22446
843	44130.82462	-3.1981	0.3675	0.7497	-0.2837	0.3028	55777
843	44171.58065	-3.0746	0.2458	0.5169	0.3916	0.2061	34578
843	44171.59016	-3.0740	0.2341	0.5149	0.4214	0.2391	33667
843	44936.54307	-2.3005	0.2043	0.3194	0.1822	0.2102	22344
843	44936.65037	-3.0870	0.2432	0.5052	0.2616	0.2453	34577
843	44936.65920	-3.0772	0.2414	0.5205	0.3958	0.2399	43467
847	44187.59606	-2.7581	0.3987	0.4901	0.3969	0.3502	34557
847	44187.60540	-2.7651	0.3930	0.5186	0.3545	0.3331	34666
847	44189.55048	-2.7952	0.4225	0.4982	0.3248	0.3698	33668
847	44189.56003	-2.7988	0.4291	0.5096	0.2621	0.3851	23569
847	44191.54832	-2.8459	0.4411	0.4812	0.3590	0.4065	33669
847	44191.55783	-2.8389	0.4527	0.5121	0.4444	0.3958	33679
847	44201.53999	-2.9831	0.4450	0.4870	0.2504	0.3559	24558
847	44201.54938	-2.9890	0.4314	0.5376	0.1662	0.3896	44779
847	44545.56849	-2.8976	0.4821	0.6089	0.1574	0.3579	25578
847	44545.57784	-2.9020	0.4738	0.5385	0.3119	0.4230	35688
847	44547.51972	-1.7594	0.5009	0.5153	0.3512	0.4070	35678
847	44547.52874	-2.9328	0.5034	0.5868	0.4855	0.3927	35579
847	44550.52146	-2.9967	0.5188	0.5078	0.4073	0.4608	45679
847	44550.53026	-2.9921	0.4897	0.5453	0.3483	0.4340	35668
847	44554.52225	-3.0104	0.4771	0.5549	0.0930	0.3693	45678
847	44554.53139	-3.0000	0.4389	0.4742	0.2362	0.3245	24657
847	44557.52307	-2.8514	0.3373	0.4617	0.2849	0.2399	35556
847	44557.53159	-2.8423	0.3261	0.3934	0.3693	0.2416	13647
847	45019.53295	-2.6549	0.2285	0.5019	0.2985	0.1970	44469
847	45019.53546	-2.6527	0.2372	0.5040	0.4039	0.2373	15569
847	45019.54418	-2.6619	0.2339	0.5134	0.3240	0.1964	13687
847	45019.54615	-2.6574	0.2334	0.5154	0.3289	0.2223	32277
847	45019.54863	-2.6756	0.2423	0.5389	0.4643	0.2087	35689
847	45314.58503	-2.3392	0.8868	0.6791	-0.0731	0.4027	24799
847	45314.59289	-2.3392	0.8412	0.5456	0.1085	0.4604	24657
847	45314.60175	-2.3432	0.8718	0.5697	0.1327	0.5204	24656
847	45316.61214	-2.6810	0.7457	0.6714	0.2676	0.5462	25678
847	45316.62416	-2.6831	0.7617	0.6834	0.1953	0.5135	44677
847	45669.59889	-2.6415	0.2320	0.4901	0.2764	0.2263	23557
847	45669.59893	-2.6476	0.2265	0.4889	0.3010	0.2239	43556
847	45669.60066	-2.6488	0.2362	0.4874	0.1476	0.2240	32668

Notes. Column 1: HV number. Column 2: HJD (-2400000.0). Column 3: Walraven V. Column 4: Walraven $V - B$. Column 5: Walraven $B - U$. Column 6: Walraven $U - W$. Column 7: Walraven $B - L$. Column 8: quality flag in the VBLUW bands, respectively. This flag indicates the internal dispersion in the photometer signal in each channel, and 0, 1, 2, ..., 9 implies, <1, 1-2, 2-4, ..., 256-512 promille variation, respectively. The full table is available at the CDS.

Table A.2. Results of the light curve fitting. Mean VBLUW photometry (first entries).

HV	V	Amp$_V$	N	B	Amp$_B$	N	L	Amp$_L$	N	U	Amp$_U$	N	W	Amp$_W$	N
824	-2.253 ± 0.015	0.145 ± 0.021	8	-2.685 ± 0.015	0.253 ± 0.030	8	-3.044 ± 0.016	0.329 ± 0.063	8	-3.230 ± 0.019	0.333 ± 0.143	8			
847	-2.860 ± 0.015	0.224 ± 0.009	30	-3.239 ± 0.025	0.293 ± 0.049	35	-3.563 ± 0.025	0.366 ± 0.052	35	-3.735 ± 0.021	0.290 ± 0.041	32	-4.140 ± 0.054	0.399 ± 0.078	15
854	-2.959 ± 0.016	0.175 ± 0.010	40	-3.231 ± 0.016	0.277 ± 0.015	40	-3.476 ± 0.016	0.351 ± 0.014	40	-3.727 ± 0.019	0.263 ± 0.028	37	-4.027 ± 0.031	0.286 ± 0.058	16
872	-2.585 ± 0.024	0.380 ± 0.020	49	-2.924 ± 0.029	0.669 ± 0.027	49									
876	-2.667 ± 0.018	0.144 ± 0.018	37	-3.107 ± 0.018	0.368 ± 0.023	37	-3.518 ± 0.025	0.532 ± 0.041	25	-3.620 ± 0.021	0.322 ± 0.026	24	-3.979 ± 0.035	0.379 ± 0.060	30
880	-2.849 ± 0.020	0.276 ± 0.018	48	-3.063 ± 0.026	0.420 ± 0.026	48	-3.296 ± 0.030	0.518 ± 0.034	48	-3.554 ± 0.027	0.397 ± 0.028	47	-3.866 ± 0.042	0.427 ± 0.048	34
899	-2.736 ± 0.015	0.137 ± 0.007	6	-3.262 ± 0.016	0.194 ± 0.009	6	-3.761 ± 0.021	0.228 ± 0.028	6	-3.880 ± 0.023	0.165 ± 0.037	6			
955	-2.883 ± 0.017	0.156 ± 0.022	32	-3.253 ± 0.018	0.312 ± 0.025	32	-3.576 ± 0.025	0.394 ± 0.045	30	-3.716 ± 0.034	0.474 ± 0.070	22	-4.103 ± 0.019	0.574 ± 0.036	12
969	-3.108 ± 0.018	0.110 ± 0.006	76	-3.466 ± 0.015	0.182 ± 0.010	76	-3.819 ± 0.016	0.308 ± 0.016	76	-3.980 ± 0.021	0.193 ± 0.021	78	-4.144 ± 0.094	0.608 ± 0.102	24
1013	-2.790 ± 0.019	0.105 ± 0.013	19	-3.276 ± 0.030	0.193 ± 0.029	19	-3.735 ± 0.122	0.282 ± 0.138	19	-3.838 ± 0.110	0.254 ± 0.125	18			
1345	-3.133 ± 0.022	0.142 ± 0.022	45	-3.445 ± 0.029	0.217 ± 0.034	45	-3.753 ± 0.035	0.301 ± 0.043	45	-3.945 ± 0.047	0.221 ± 0.055	43	-4.207 ± 0.245	0.161 ± 0.276	15
1374	-3.393 ± 0.037	0.169 ± 0.051	13	-3.695 ± 0.040	0.260 ± 0.058	13	-4.015 ± 0.045	0.378 ± 0.066	12	-4.141 ± 0.031	0.230 ± 0.037	10			
1610	-2.960 ± 0.027	0.492 ± 0.025	13							-3.671 ± 0.093	0.346 ± 0.098	13			
1618	-3.393 ± 0.016	0.164 ± 0.012	51	-3.622 ± 0.016	0.243 ± 0.017	51	-3.819 ± 0.019	0.271 ± 0.025	51	-4.034 ± 0.024	0.175 ± 0.045	21			
1705	-3.337 ± 0.016	0.092 ± 0.014	13	-3.680 ± 0.016	0.134 ± 0.015	13	-4.026 ± 0.030	0.217 ± 0.065	12	-4.104 ± 0.039	0.315 ± 0.043	7			
1744	-3.077 ± 0.015	0.148 ± 0.010	80	-3.347 ± 0.016	0.225 ± 0.013	80	-3.590 ± 0.017	0.273 ± 0.021	79	-3.814 ± 0.020	0.232 ± 0.033	49	-4.120 ± 0.056	0.253 ± 0.076	17
1768	-3.265 ± 0.042	0.162 ± 0.047	16	-3.543 ± 0.064	0.189 ± 0.074	16	-3.809 ± 0.101	0.384 ± 0.118	16	-4.032 ± 0.109	0.183 ± 0.130	15			
1884	-2.975 ± 0.027	0.218 ± 0.029	7	-3.302 ± 0.025	0.317 ± 0.026	7	-3.597 ± 0.044	0.421 ± 0.053	7	-3.796 ± 0.044	0.323 ± 0.052	6			
1967	-2.633 ± 0.023	0.283 ± 0.040	22	-3.009 ± 0.021	0.265 ± 0.038	22	-3.331 ± 0.023	0.321 ± 0.046	21	-3.531 ± 0.026	0.269 ± 0.057	22	-3.845 ± 0.028	0.302 ± 0.065	8
2063	-3.227 ± 0.018	0.179 ± 0.013	40	-3.540 ± 0.016	0.225 ± 0.009	40	-3.902 ± 0.026	0.360 ± 0.027	32	-3.688 ± 0.241	0.609 ± 0.250	15			
2205	-2.909 ± 0.023	0.198 ± 0.033	28	-3.328 ± 0.021	0.380 ± 0.031	28	-3.747 ± 0.021	0.583 ± 0.026	24	-3.891 ± 0.026	0.429 ± 0.033	28			
2209	-2.679 ± 0.019	0.124 ± 0.006	56	-2.958 ± 0.015	0.197 ± 0.011	56	-3.217 ± 0.016	0.254 ± 0.045	29	-3.451 ± 0.016	0.180 ± 0.016	27	-3.788 ± 0.019	0.195 ± 0.032	18
2249	-2.825 ± 0.017	0.269 ± 0.023	58	-3.153 ± 0.020	0.415 ± 0.038	58	-3.471 ± 0.021	0.493 ± 0.045	58	-3.715 ± 0.021	0.350 ± 0.040	52	-4.001 ± 0.028	0.370 ± 0.051	35
2260	-3.211 ± 0.015	0.163 ± 0.009	52	-3.623 ± 0.016	0.253 ± 0.016	52	-4.026 ± 0.018	0.384 ± 0.024	52	-4.166 ± 0.019	0.302 ± 0.031	38			
2299	-2.932 ± 0.017	0.161 ± 0.011	92	-3.267 ± 0.020	0.264 ± 0.018	92	-3.578 ± 0.025	0.335 ± 0.025	93	-3.774 ± 0.025	0.263 ± 0.025	91	-4.194 ± 0.032	0.635 ± 0.031	6
2454	-3.014 ± 0.018	0.152 ± 0.026	56	-3.533 ± 0.020	0.273 ± 0.040	56	-4.020 ± 0.021	0.474 ± 0.059	56	-4.182 ± 0.027	0.416 ± 0.087	48	-3.983 ± 0.041	0.163 ± 0.048	50
2680	-3.163 ± 0.016	0.133 ± 0.016	39	-3.505 ± 0.016	0.218 ± 0.021	39	-3.868 ± 0.021	0.338 ± 0.035	39	-3.998 ± 0.020	0.245 ± 0.048	33			
2686	-3.422 ± 0.017	0.140 ± 0.015	25	-3.751 ± 0.018	0.233 ± 0.024	25	-4.202 ± 0.048	0.450 ± 0.058	22	-4.230 ± 0.039	0.114 ± 0.088	19			
5655	-3.090 ± 0.020	0.169 ± 0.045	46	-3.532 ± 0.017	0.345 ± 0.028	46	-3.930 ± 0.022	0.535 ± 0.074	42	-4.139 ± 0.021	0.415 ± 0.060	37	-4.363 ± 0.032	0.307 ± 0.053	24
270100	-1.951 ± 0.015	0.091 ± 0.003	47	-2.426 ± 0.015	0.170 ± 0.007	47	-2.852 ± 0.015	0.251 ± 0.010	42	-2.977 ± 0.015	0.186 ± 0.010	37	-3.491 ± 0.018	0.220 ± 0.027	26
817	-2.802 ± 0.017	0.164 ± 0.019	34	-3.080 ± 0.017	0.251 ± 0.022	34	-3.322 ± 0.018	0.292 ± 0.031	34	-3.440 ± 0.051	0.158 ± 0.098	29			
821	-2.041 ± 0.017	0.131 ± 0.020	34	-2.514 ± 0.017	0.259 ± 0.020	34	-2.945 ± 0.022	0.341 ± 0.040	29	-3.079 ± 0.018	0.285 ± 0.030	23			
822	-3.110 ± 0.020	0.228 ± 0.041	15	-3.469 ± 0.018	0.289 ± 0.029	15	-3.785 ± 0.236	0.481 ± 0.451	14	-3.848 ± 0.034	0.346 ± 0.088	10			
823	-2.755 ± 0.017	0.169 ± 0.022	21	-3.176 ± 0.019	0.277 ± 0.031	21	-3.455 ± 0.022	0.307 ± 0.044	20	-3.637 ± 0.042	0.261 ± 0.094	13			
827	-3.046 ± 0.017	0.139 ± 0.020	33	-3.308 ± 0.016	0.220 ± 0.016	33	-3.532 ± 0.020	0.236 ± 0.036	32	-3.747 ± 0.021	0.210 ± 0.044	22			
829	-2.029 ± 0.015	0.130 ± 0.011	33	-2.406 ± 0.016	0.215 ± 0.012	33	-2.734 ± 0.018	0.259 ± 0.029	31	-2.909 ± 0.019	0.235 ± 0.035	26			
834	-2.138 ± 0.016	0.111 ± 0.013	43	-2.529 ± 0.017	0.217 ± 0.024	41	-2.864 ± 0.017	0.319 ± 0.025	41	-3.024 ± 0.018	0.248 ± 0.030	28			
837	-2.568 ± 0.016	0.171 ± 0.013	36	-2.979 ± 0.016	0.271 ± 0.020	36	-3.315 ± 0.017	0.323 ± 0.024	37	-3.468 ± 0.019	0.284 ± 0.032	25			
877	-2.606 ± 0.016	0.127 ± 0.016	22	-3.183 ± 0.016	0.218 ± 0.017	22	-3.640 ± 0.021	0.256 ± 0.041	22	-3.720 ± 0.021	0.281 ± 0.041	23			
883	-2.130 ± 0.016	0.206 ± 0.015	28	-2.735 ± 0.017	0.337 ± 0.019	28	-3.188 ± 0.021	0.374 ± 0.044	28	-3.282 ± 0.018	0.343 ± 0.028	11			
886	-2.607 ± 0.017	0.219 ± 0.028	20	-3.014 ± 0.018	0.396 ± 0.028	20	-3.166 ± 0.025	0.566 ± 0.039	17	-3.566 ± 0.023	0.458 ± 0.049	21			
900	-2.391 ± 0.017	0.183 ± 0.024	22	-2.855 ± 0.020	0.306 ± 0.037	22	-3.246 ± 0.022	0.413 ± 0.048	21	-3.399 ± 0.022	0.380 ± 0.045	13			
902	-2.596 ± 0.017	0.189 ± 0.022	21	-2.990 ± 0.021	0.317 ± 0.039	21	-3.425 ± 0.019	0.490 ± 0.035	19	-3.506 ± 0.043	0.381 ± 0.096	17			
909	-2.369 ± 0.017	0.207 ± 0.023	29	-2.767 ± 0.018	0.357 ± 0.025	29	-3.138 ± 0.019	0.469 ± 0.030	26	-3.303 ± 0.021	0.405 ± 0.038	13			
953	-2.187 ± 0.017	0.178 ± 0.022	22	-2.617 ± 0.018	0.301 ± 0.030	22	-2.986 ± 0.018	0.369 ± 0.026	17	-3.155 ± 0.032	0.347 ± 0.074	26			
1002	-2.438 ± 0.018	0.201 ± 0.031	30	-2.855 ± 0.019	0.332 ± 0.032	30	-3.195 ± 0.019	0.496 ± 0.041	15	-3.392 ± 0.041	0.377 ± 0.043	17			
1003	-2.569 ± 0.018	0.209 ± 0.028	25	-2.932 ± 0.018	0.331 ± 0.028	25	-3.274 ± 0.019	0.424 ± 0.031	18	-3.415 ± 0.021	0.316 ± 0.040	15			
1365	-3.291 ± 0.017	0.138 ± 0.019	42	-3.584 ± 0.017	0.212 ± 0.020	42	-3.808 ± 0.018	0.214 ± 0.028	39	-4.022 ± 0.025	0.164 ± 0.060	31			

Notes. Column 1: HV number; 270100 refers to HDE 270100 (van Genderen & Nitihardjo 1989). Column 2-11: Mean values and amplitudes with error bars and the number of data points in the VBLUW filters. The full table is available at the CDS.

Appendix B: Mass estimates

Table B.1 compiles the mass estimates using the different methods outlined in the main text (also see the table footnote). The adopted mass is the median among the five estimates. To estimate the error bar the error in the mass estimate of the median value is added in quadrature to the median-absolute-deviation times 1.48 (to get the equivalent of one sigma in a Gaussian distribution) among the five estimates.

Table B.1. Stellar mass estimates (selected entries only).

Identifier	Period (d)	M_1 ($M_\odot$)	M_2 ($M_\odot$)	M_3 ($M_\odot$)	M_4 ($M_\odot$)	M_5 ($M_\odot$)	M_{adopted} ($M_\odot$)
LMC3004	1.52	2.50 ± 0.01	2.81 ± 0.01	2.94 ± 0.02	2.84 ± 0.08	2.17 ± 0.01	2.81 ± 0.13
LMC1523	1.57	2.64 ± 0.01	2.81 ± 0.01	3.03 ± 0.02	2.91 ± 0.09	2.45 ± 0.01	2.81 ± 0.17
LMC3724	2.64	3.41 ± 0.01	3.91 ± 0.01	3.96 ± 0.03	3.63 ± 0.14	3.21 ± 0.01	3.63 ± 0.34
LMC3750	2.95	3.37 ± 0.01	3.81 ± 0.01	3.86 ± 0.04	3.55 ± 0.13	3.32 ± 0.01	3.55 ± 0.30
LMC2138	3.01	3.48 ± 0.01	3.82 ± 0.01	3.94 ± 0.03	3.61 ± 0.13	3.25 ± 0.01	3.61 ± 0.29
LMC3744	3.05	3.86 ± 0.01	4.41 ± 0.01	4.46 ± 0.01	4.01 ± 0.17	2.08 ± 0.01	4.01 ± 0.47
LMC4646	3.10	3.82 ± 0.01	4.47 ± 0.01	4.45 ± 0.04	4.00 ± 0.17	3.68 ± 0.01	4.00 ± 0.41
LMC3723	3.14	3.58 ± 0.01	4.16 ± 0.01	4.15 ± 0.04	3.77 ± 0.15	3.33 ± 0.01	3.77 ± 0.44
LMC3756	3.21	3.47 ± 0.01	3.78 ± 0.01	3.90 ± 0.04	3.57 ± 0.13	3.46 ± 0.01	3.57 ± 0.23
LMC3752	3.44	3.59 ± 0.01	3.79 ± 0.01	3.96 ± 0.04	3.62 ± 0.14	3.63 ± 0.01	3.63 ± 0.07
LMC3726	3.52	3.59 ± 0.01	4.11 ± 0.01	4.10 ± 0.04	3.73 ± 0.14	3.50 ± 0.01	3.73 ± 0.31
LMC0961	3.71	4.01 ± 0.01	4.49 ± 0.01	4.55 ± 0.03	4.06 ± 0.17	3.26 ± 0.01	4.06 ± 0.50
LMC1124	4.46	3.88 ± 0.01	4.35 ± 0.01	4.34 ± 0.05	3.90 ± 0.16	3.89 ± 0.01	3.90 ± 0.23
LMC3320	4.79	4.35 ± 0.01	4.75 ± 0.01	4.81 ± 0.06	4.25 ± 0.19	4.27 ± 0.01	4.35 ± 0.10
SMC3588	5.32	4.85 ± 0.02	5.29 ± 0.01	5.35 ± 0.07	4.64 ± 0.22	4.57 ± 0.02	4.85 ± 0.27
SMC2254	5.65	6.00 ± 0.02	6.64 ± 0.02	6.69 ± 0.10	5.61 ± 0.33	5.58 ± 0.03	6.00 ± 0.42
LMC1939	6.06	4.53 ± 0.02	4.98 ± 0.01	4.97 ± 0.06	4.36 ± 0.20	4.31 ± 0.02	4.53 ± 0.22
LMC1466	6.15	4.27 ± 0.01	4.80 ± 0.01	4.72 ± 0.06	4.17 ± 0.18	4.21 ± 0.02	4.27 ± 0.11
LMC0594	6.73	4.62 ± 0.02	5.02 ± 0.01	5.01 ± 0.08	4.38 ± 0.20	4.90 ± 0.02	4.90 ± 0.17
LMC1526	6.73	4.47 ± 0.02	4.71 ± 0.01	4.77 ± 0.07	4.21 ± 0.18	4.67 ± 0.01	4.67 ± 0.15
LMC1424	6.78	4.13 ± 0.01	4.86 ± 0.01	4.62 ± 0.05	4.09 ± 0.17	3.93 ± 0.02	4.13 ± 0.19
LMC1941	6.81	5.04 ± 0.02	6.25 ± 0.01	5.82 ± 0.07	4.97 ± 0.26	4.67 ± 0.03	5.04 ± 0.37
LMC1313	6.83	4.39 ± 0.02	4.60 ± 0.01	4.67 ± 0.07	4.13 ± 0.18	4.50 ± 0.01	4.50 ± 0.15
LMC1128	6.86	4.53 ± 0.02	4.76 ± 0.01	4.83 ± 0.07	4.25 ± 0.19	4.60 ± 0.01	4.60 ± 0.19
LMC1374	6.89	4.17 ± 0.01	4.61 ± 0.01	4.53 ± 0.06	4.02 ± 0.17	4.27 ± 0.01	4.27 ± 0.26
LMC1327	6.92	4.37 ± 0.01	4.70 ± 0.01	4.70 ± 0.07	4.15 ± 0.18	4.55 ± 0.01	4.55 ± 0.18
. . .							
LMC1113	37.56	8.57 ± 0.04	8.83 ± 0.02	8.39 ± 0.33	6.63 ± 0.45	10.14 ± 0.05	8.57 ± 0.27
LMC3158	39.19	3.83 ± 0.01	3.62 ± 0.01	3.48 ± 0.08	3.15 ± 0.10	4.88 ± 0.01	3.62 ± 0.20
SMC2706	39.20	7.81 ± 0.04	8.76 ± 0.02	7.90 ± 0.24	6.30 ± 0.41	8.64 ± 0.05	7.90 ± 0.75
LMC0512	39.40	8.40 ± 0.04	8.88 ± 0.02	8.29 ± 0.33	6.56 ± 0.44	10.17 ± 0.05	8.40 ± 0.48
SMC1797	41.21	7.70 ± 0.04	8.87 ± 0.02	7.85 ± 0.22	6.26 ± 0.41	8.31 ± 0.05	7.85 ± 0.46
SMC4444	41.83	9.90 ± 0.06	10.22 ± 0.03	9.69 ± 0.43	7.49 ± 0.58	11.60 ± 0.07	9.90 ± 0.33
LMC0943	42.24	9.64 ± 0.06	10.24 ± 0.03	9.54 ± 0.41	7.39 ± 0.56	11.24 ± 0.07	9.64 ± 0.60
SMC2470	42.75	9.09 ± 0.05	9.59 ± 0.02	8.95 ± 0.34	6.99 ± 0.51	10.27 ± 0.06	9.09 ± 0.50
LMC0461	45.17	7.77 ± 0.04	8.86 ± 0.02	7.85 ± 0.24	6.25 ± 0.40	8.55 ± 0.05	7.85 ± 0.70
LMC0966	47.38	9.33 ± 0.05	10.06 ± 0.03	9.22 ± 0.33	7.17 ± 0.53	10.13 ± 0.07	9.33 ± 0.74
LMC4663	47.96	10.96 ± 0.07	11.24 ± 0.03	10.65 ± 0.50	8.10 ± 0.68	12.51 ± 0.08	10.96 ± 0.33
LMC1290	48.38	10.00 ± 0.06	10.48 ± 0.03	9.77 ± 0.70	7.53 ± 0.58	14.69 ± 0.07	10.00 ± 0.49
LMC2253	52.37	9.24 ± 0.05	9.85 ± 0.03	9.03 ± 0.36	7.03 ± 0.51	10.62 ± 0.06	9.24 ± 0.61
LMC0992	52.87	10.61 ± 0.07	10.39 ± 0.03	10.02 ± 0.47	7.68 ± 0.61	12.04 ± 0.07	10.39 ± 0.38
SMC0921	65.94	10.12 ± 0.06	9.91 ± 0.03	9.42 ± 0.62	7.27 ± 0.55	13.83 ± 0.06	9.91 ± 0.50
SMC2099	73.62	13.14 ± 0.10	13.46 ± 0.05	12.53 ± 0.66	9.24 ± 0.88	14.30 ± 0.12	13.14 ± 0.63
LMC4691	73.90	12.24 ± 0.09	12.45 ± 0.04	11.60 ± 0.61	8.66 ± 0.77	13.72 ± 0.10	12.24 ± 0.66
LMC4689	78.51	10.54 ± 0.07	12.02 ± 0.03	10.42 ± 0.46	7.90 ± 0.64	11.92 ± 0.10	10.54 ± 1.39
SMC1502	84.30	12.27 ± 0.09	11.90 ± 0.04	11.29 ± 0.76	8.45 ± 0.74	15.35 ± 0.09	11.90 ± 0.62
LMC4628	99.20	13.56 ± 0.11	14.88 ± 0.05	13.12 ± 0.83	9.57 ± 0.95	16.03 ± 0.15	13.56 ± 1.33
LMC4629	108.70	6.77 ± 0.03	6.86 ± 0.01	6.12 ± 0.33	5.01 ± 0.26	10.05 ± 0.03	(6.77 ± 0.66)
LMC1591	118.62	9.50 ± 0.05	9.84 ± 0.02	8.74 ± 0.39	6.77 ± 0.47	11.02 ± 0.06	(9.50 ± 0.76)
SMC0417	128.20	6.71 ± 0.03	6.02 ± 0.01	5.68 ± 0.62	4.69 ± 0.23	13.83 ± 0.02	(6.02 ± 0.70)
LMC0619	133.78	8.74 ± 0.05	9.18 ± 0.02	8.00 ± 0.21	6.28 ± 0.41	8.03 ± 0.06	(8.03 ± 0.77)
SMC3611	208.80	9.60 ± 0.05	10.39 ± 0.02	8.71 ± 0.33	6.71 ± 0.46	10.14 ± 0.07	(9.60 ± 0.79)

Notes. Column 1: Identifier (sources are sorted by period). Column 2: Period. Column 3: Mass estimate from the period-luminosity-mass-effective temperature-metallicity relation derived in Groenewegen & Jurkovic (2017) based on the models in Bono et al. (2000b). Column 4: Mass estimate from Eq. 1, based on the models of Anderson et al. (2016). Column 5: Mass estimate from the relation in Ragosta et al. (2019). Column 6: Mass estimate from the relation in Pilecki et al. (2018). Column 7: Mass estimate from the relation in Marconi et al. (2020). Column 8: Adopted mass based on the median and the MAD (see text). Values between parenthesis are deemed unreliable and have not been used in the analysis of the mass-luminosity relation and in the calculation of the evolutionary $\log g$ and FWG values. The full table is available at the CDS.

Appendix C: 2D Cepheid model

Vasilyev et al. (2017, 2018) present the results of a two-dimensional time-dependent envelope model of a CC with $T_{\rm eff}$ = 5600 K and $\log g_0$ = 2.0 dex. In Figure 5 of Vasilyev et al. (2017), the term $g_0 + \frac{\partial v}{\partial t}$ is plotted against time. The time series of various quantities were kindly made available, and are plotted in a slightly different way in Fig. C.1. A Fourier analysis of the velocity time series showed a periodicity of 2.6426 days (and a mean of -7.86 km s^{-1}), which is used to phase the data. Phase zero is taken at the instance in time when the normalised flux reaches a maximum for the first time. Consecutive pulsation cycles are plotted with different colours. The cycles are not very smooth. This is explained by convection, which adds statistical fluctuations to the velocity and thermal structure of their model (Sect. 2.1 in Vasilyev et al. 2017).

The integral of the velocity curve is used to calculate the change in radius. For a mass of 3 $M_\odot$, $\log g$ = 2.0 dex implies a radius of about 29 $R_\odot$. The top panel shows how $g_{\rm eff}$ changes over the pulsation cycle. The effective gravity is below 100 for 68% of the time, with an average value of 66 cm/s^2 (-0.18 dex), and above 100 cm/s^2 32% of the time for an average of 166 (+0.22 dex). The 5 and 95% percentiles correspond to values of ± 0.35 dex. The effect of the change in radius is almost negligible (of order 5-10 cm/s^2, or ± 0.04 dex at most) compared to the derivative of the velocity in determining $g_{\rm eff}$.
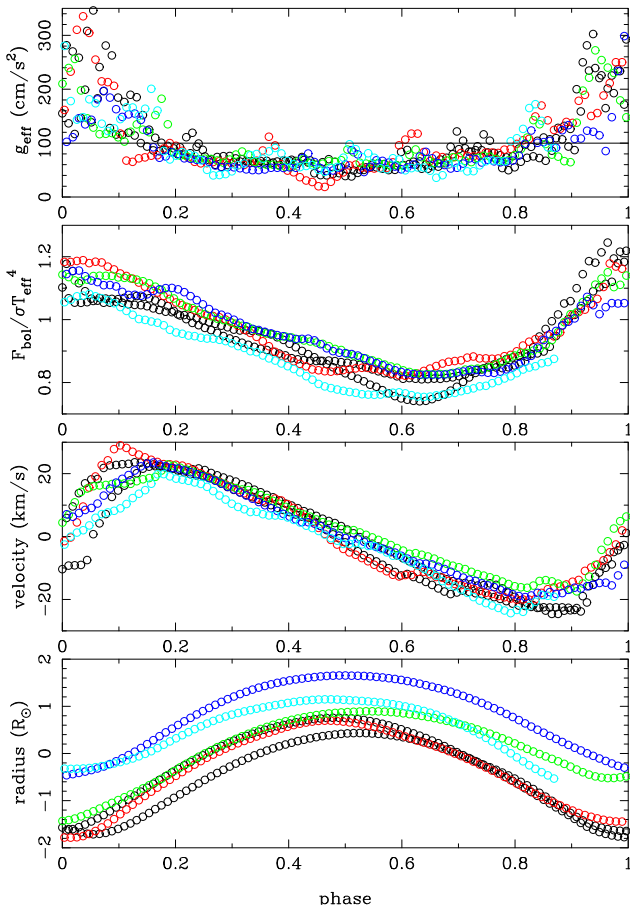
Fig. C.1. Various quantities plotted against phase based on the 2D models of Vasilyev et al. (2017, 2018). Different pulsation cycles are plotted in different colours. From top to bottom, the effective gravity, normalised flux, velocity and change in radius. See text for details.
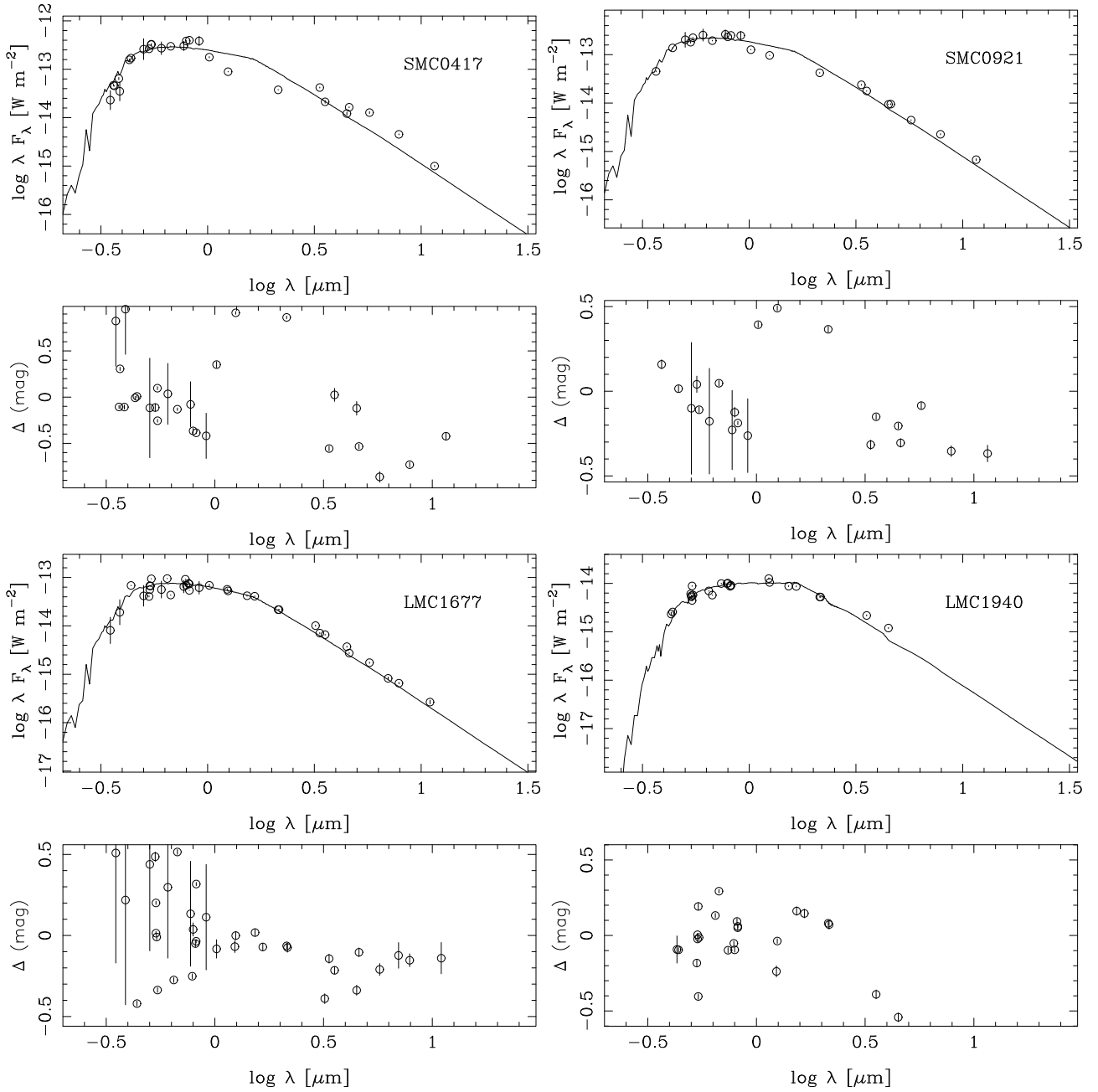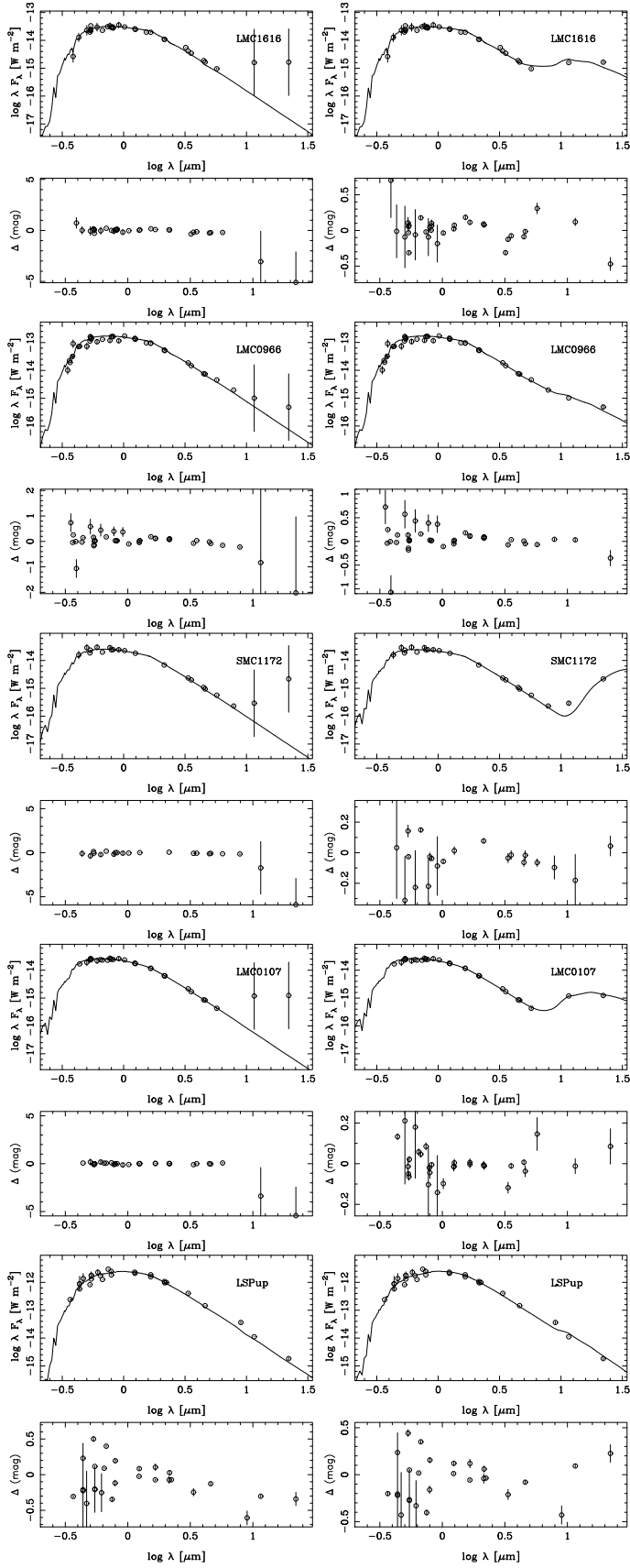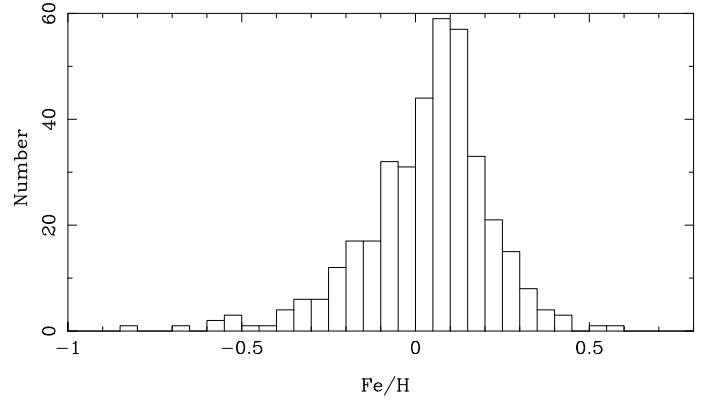
Appendix D: Additional figures

Fig. D.1. Details as in Fig. 1 for the four poorest-fitting models.

Fig. D.2. Models without dust (left-hand side) with dust (right-hand side) for the five MC stars where the dust excess is unlikely to be related to the star, and the model for the MW star LS Pup for comparison.

Fig. D.3. Distribution in [Fe/H] of the 380 galactic CC used in G20 to determine the PL and PR relations.
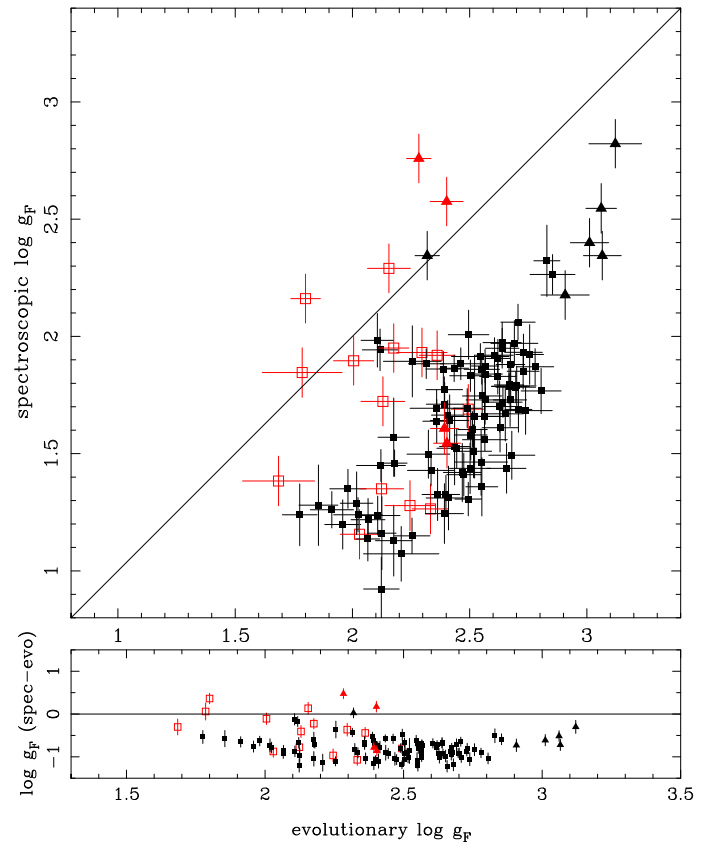
Fig. D.4. FWG determined from the SED fitting and the derived stellar mass compared to that from spectroscopic temperature and gravity determination from the literature. Symbols as in Fig. 9. The median offset is -0.79 ± 0.24 dex.
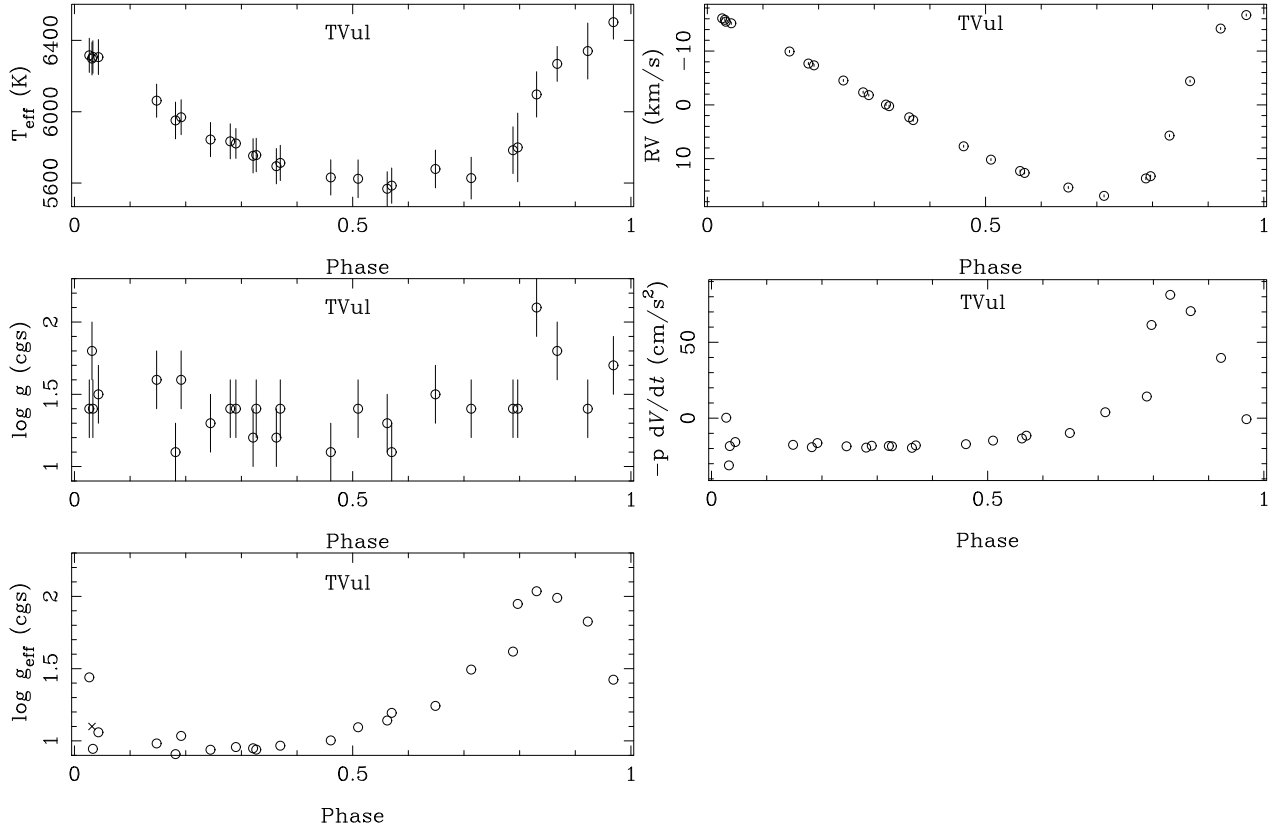
Fig. D.5. Same as Fig. 11, but for T Vul.
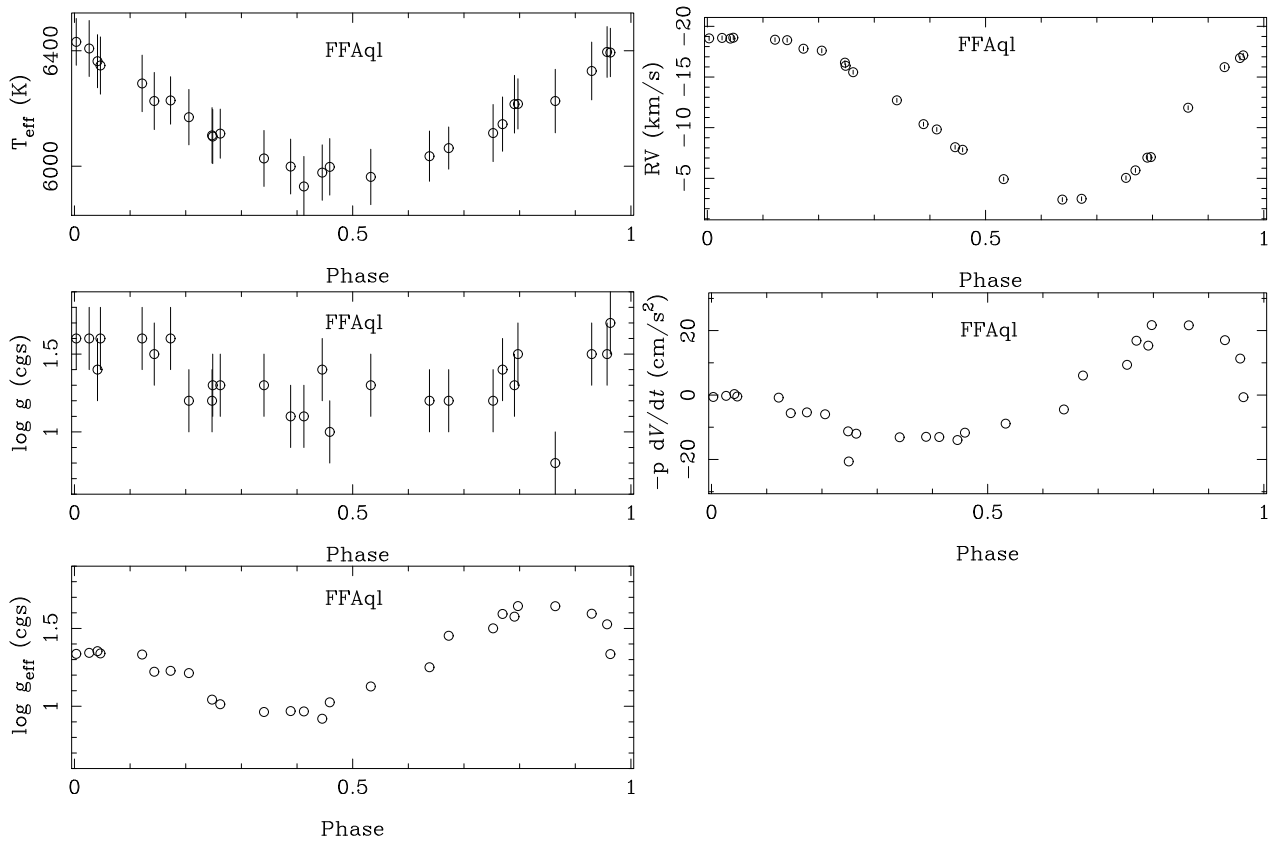
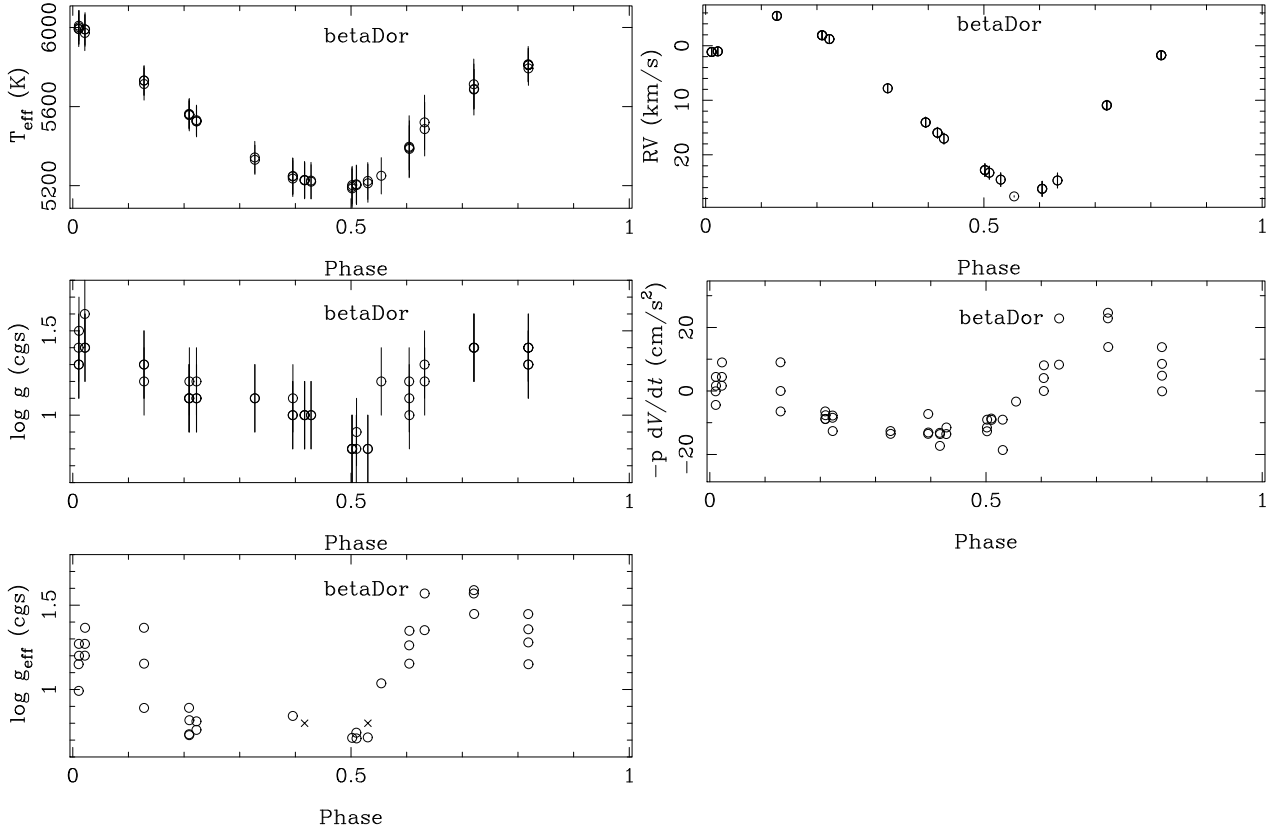**Fig. D.6.** Same as Fig. 11, but for FF Aql.

Fig. D.7. Same as Fig. 11, but for β Dor. Effective gravities below zero are unphysical and are plotted with a cross at the lowest observed log g.
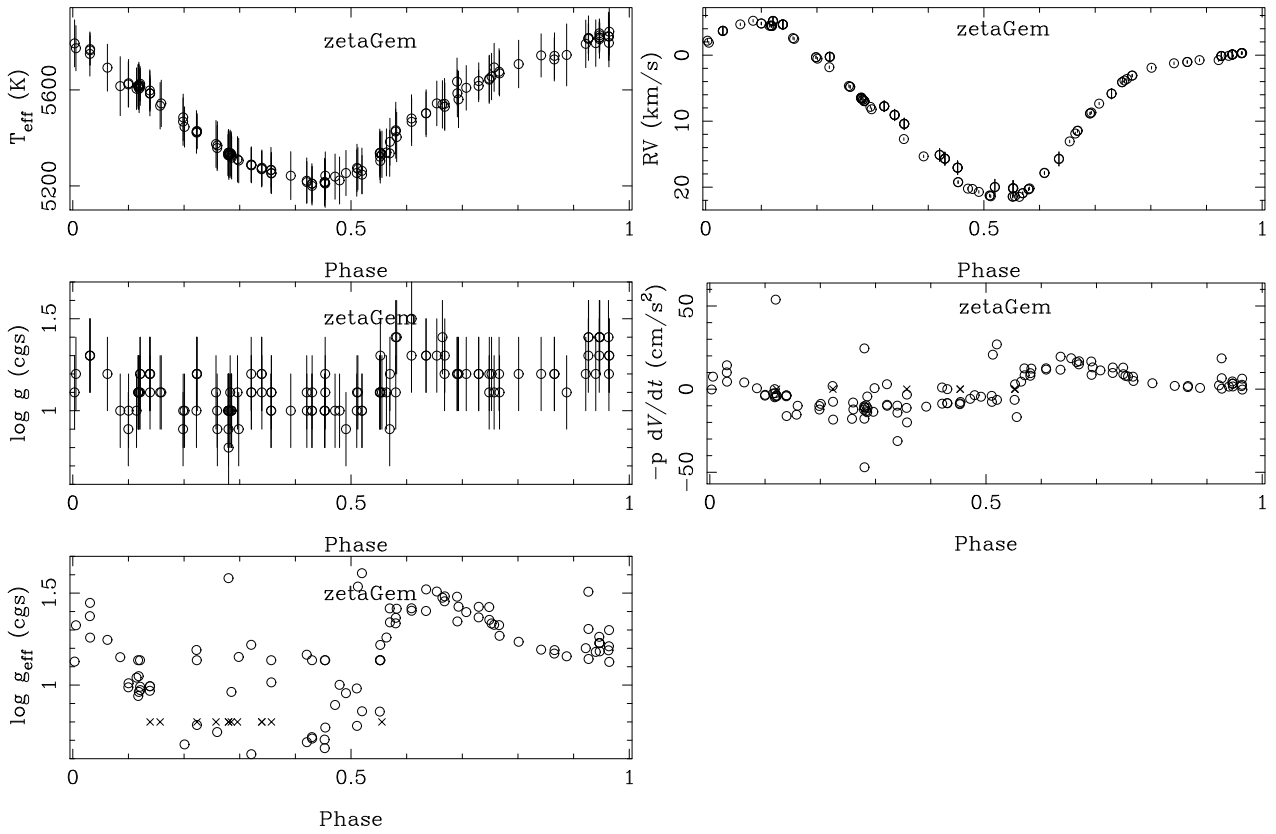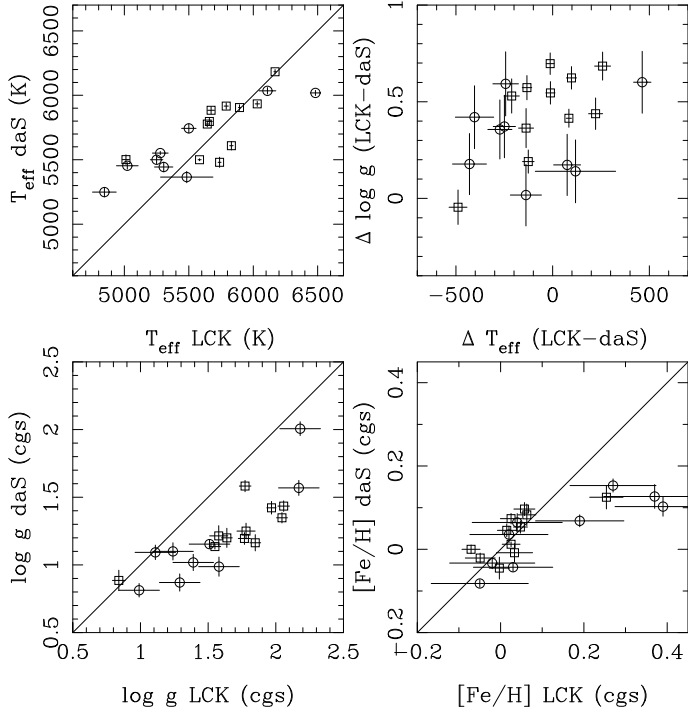

Fig. D.8. Same as Fig. 11, but for ζ Gem. Dynamical terms larger than 50 cm/s² in absolute values are discarded and plotted with a cross. Effective gravities below zero are unphysical and are plotted with a cross at the lowest observed log g.

Fig. D.9. Comparison between Luck (2018) (LCK) and da Silva et al. (2022) (daS) in terms of effective temperature, $\log g$, the differential between the two, and iron abundance. The stars with only one spectrum in Luck (2018) are marked by circles, objects plotted with squares have 5 or more spectra. Abundances in Luck (2018) are given on a scale where log Hydrogen abundance = 12 and have been converted to the scale in da Silva et al. (2022) using their adopted iron abundance of log Fe = 7.50.